Deciphering the hidden structures of HH 216 and Pillar IV in M16: results from *JWST* and *HST*

L. K. Dewangan [1]★ O. R. Jadhav [1,2] A. K. Maity [1,2] N. K. Bhadari [1] Saurabh Sharma [3] M. Padovani [4] T. Baug [5] Y. D. Mayya [6] and Rakesh Pandey [1]

[1]*Physical Research Laboratory, Navrangpura, Ahmedabad - 380 009, India*
[2]*Indian Institute of Technology Gandhinagar Palaj, Gandhinagar 382355, India*
[3]*Aryabhatta Research Institute of Observational Sciences, Manora Peak, Nainital 263002, India*
[4]*INAF–Osservatorio Astrofisico di Arcetri, Largo E. Fermi 5, I-50125 Firenze, Italy*
[5]*S. N. Bose National Centre for Basic Sciences, Sector-III, Salt Lake, Kolkata 700106, India*
[6]*Instituto Nacional de Astrofísica, Óptica y Electrónica, Luis Enrique Erro # 1, Tonantzintla, Puebla, C.P. 72840, México*

ABSTRACT

To probe the star formation process, we present an observational investigation of the Pillar IV and an ionized knot HH 216 in the Eagle Nebula (M16). Pillar IV is known to host a Class I protostar that drives a bipolar outflow. The outflow has produced the bow shock, HH 216, which is associated with the red-shifted outflow lobe. The JWST near- and mid-infrared images (resolution $\sim 0''.07$–$0''.7$) reveal the protostar as a single, isolated object (below 1000 au). The outer boundary of Pillar IV is depicted with the 3.3 μm Polycyclic aromatic hydrocarbon (PAH) emission. HH 216 is traced with the 4.05 μm Brα and the radio continuum emission; however, it is undetected with 4.693 μm H_2 emission. HH 216 seems to be associated with both thermal and non-thermal radio emissions. High-resolution images reveal entangled ionized structures (below 3000 au) of HH 216, which appear to be located towards termination shocks. New knots in 4.693 μm H_2 emission are detected and are mainly found on Pillar IV's northern side. This particular result supports the previously proposed episodic accretion in the powering source of HH 216. One part of the ionized jet (extent ~ 0.16 pc) is discovered on the southern side of the driving source. Using the $^{12}CO(J = 1$–$0)$, $^{12}CO(J = 3$–$2)$, and $^{13}CO(J = 1$–$0)$ emission, observational signposts of cloud-cloud collision (or interacting clouds) towards Pillar IV are investigated. Overall, our results suggest that the interaction of molecular cloud components around 23 and 26 km s^{-1} might have influenced star formation activity in Pillar IV.

Key words: stars: formation – stars: pre-main sequence – ISM: clouds – dust, extinction – HII regions – ISM: individual object (HH 216): ISM: kinematics and dynamics.

1 INTRODUCTION

High-resolution and high-sensitivity near-infrared (NIR) and mid-infrared (MIR) observations from the James Webb Space Telescope (*JWST*) allow the study of the dust and gaseous structures around embedded protostars. This can enable us to gain a better understanding of physical processes taking place in star-forming sites (e.g. Pontoppidan et al. 2022). The *JWST* facility has mapped the 'Pillars of Creation' or 'elephant trunks' in the Eagle Nebula (M16), which has been regarded as a site of active star formation. This argument is supported by the presence of one interesting and well recognized source, Herbig-Haro (HH) 216 (hereafter HH 216), that is the bow shock of a bipolar jet (e.g. Meaburn & White 1982; Andersen et al. 2004; Oliveira 2008; Flagey et al. 2020). There is also evidence of the episodic accretion in the powering source of HH 216 (e.g. Flagey et al. 2020). In this paper, we have re-examined the *JWST* NIR and MIR images towards HH 216 (see Fig. 1) to understand the underlying physical processes.

Eagle Nebula or M16 hosts the optical cluster NGC 6611, and is one of well-studied star-forming sites. Eagle Nebula is powered by the hot stars in the cluster NGC 6611, which are responsible for heating and ionizing the Nebula (i.e. M16 HII region). On the basis of GAIA parallax observations, Kuhn et al. (2019) estimated a distance of 1.74 ± 0.13 kpc to NGC 6611, which is used in this paper (see also Karim et al. 2023). The collision between two molecular cloud components has been proposed to explain the existence of O-type stars in this cluster (Nishimura et al. 2021). Using the Hubble Space Telescope (*HST*) data, it is investigated that M16 contains Pillars of neutral gas, which have been referred to as 'Pillars of Creation' or 'elephant trunks' (see Hester et al. 1996, for more details). These Pillars (labelled as I, II, III, and IV; see fig. 1 of Oliveira 2008) are associated with signs of ongoing star formation (e.g. White et al. 1999; Indebetouw et al. 2007; Oliveira 2008; Sofue 2020). Using the photometry data at 1–8 μm, Indebetouw et al. (2007) identified candidate young stellar objects (YSOs) in the Eagle Nebula. They suggested that the Pillars might have been influenced by the feedback of massive stars; however, spontaneous star formation was proposed in the dense parts of these Pillars.

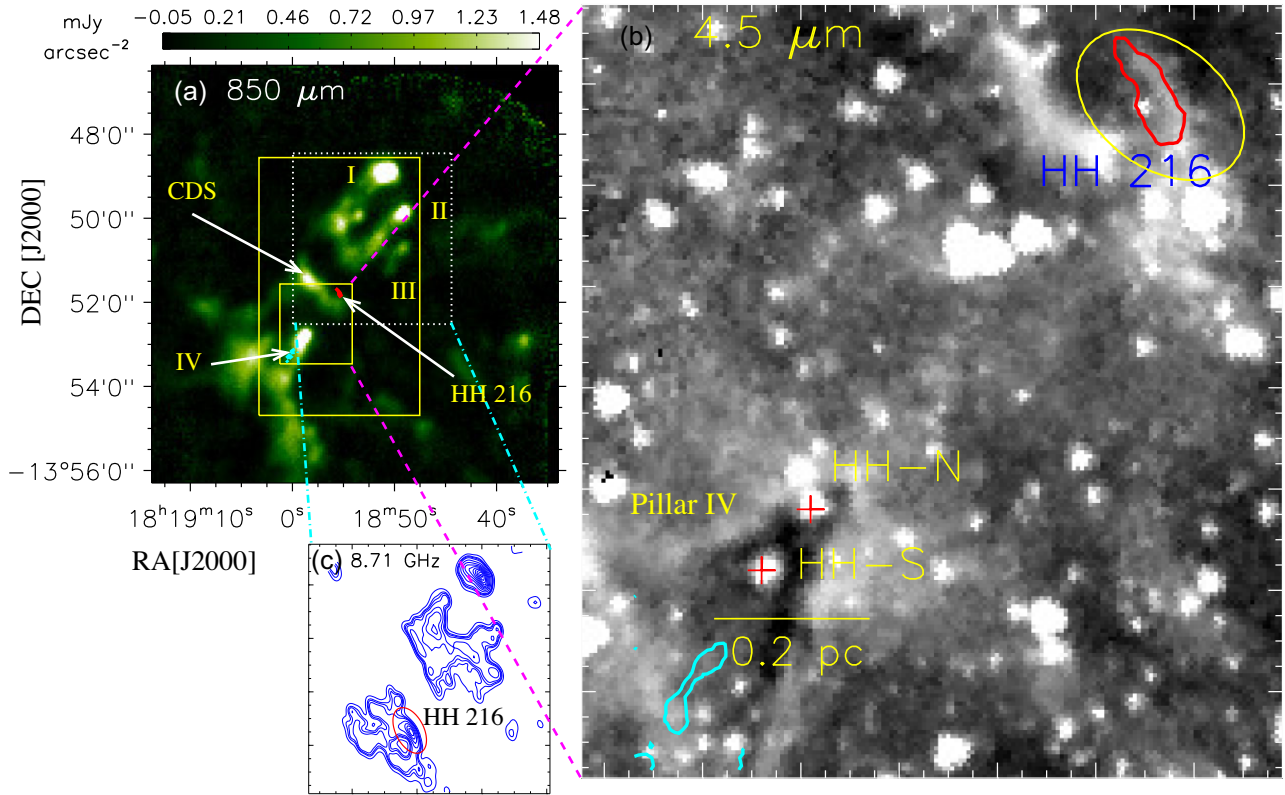★ E-mail: loku007@gmail.com; lokeshd@prl.res.in

Figure 1. An 850 μm dust emission map of the 'Pillars of Creation' (also known as Eagle Nebula, or Messier 16) obtained using SCUBA-2 on the JCMT. Pillars, HH 216, and 'central dense structure' ('CDS') are labelled. The solid box highlights the area shown in Fig. 1(b), while the dotted box encompasses the area presented in Fig. 1(c). The dot–dashed box highlights the area shown in Figs 2(a) and (b). (b) *Spitzer* 4.5 μm image. The outflow signature (i.e. red and cyan lobes from the Hα radial velocity map; see curves and also Flagey et al. (2020)) is indicated. A scale bar corresponding to 0.2 pc (at a distance of 1.74 kpc) and two objects (i.e. HH-N and HH-S; see cross symbols) are presented. (c) Radio 8.71 GHz continuum emission contours. The levels of the contours are 30.5 mJy beam^{-1} × (0.036, 0.07, 0.09, 0.12, 0.2, 0.3, 0.4, 0.5, 0.6, 0.7, 0.8, 0.9, and 0.98). Pillar IV is indicated in panels 'a' and 'b'. In panels 'b' and 'c', the ellipse shows the location of HH 216.

The interesting object HH 216 (or M16-HH1) was identified in the Hα radial velocity map (Meaburn & White 1982; Andersen et al. 2004; Flagey et al. 2020) and also in the radio 8.7 GHz continuum emission (see fig. 2d of White et al. 1999). Using the optical nebular emission lines (i.e. [O II]λ3726,29, Hβ, [O III]λ4959,5007, [N II]λ6548,84, Hα, and [S II]λ6717,31) around HH 216, Flagey et al. (2020) detected several knots, bipolar structure of the flow (extent ∼1.8 pc at a distance of 2.0 kpc), and likely powering source (see also Andersen et al. 2004; Indebetouw et al. 2007; Oliveira 2008; Karim et al. 2023). These results were together considered signatures of the episodic accretion in the driving source of the HH 216 outflow that is located at the tip of the Pillar IV (see fig. 13 of Flagey et al. 2020). Apart from the embedded source, two objects (i.e. HH-N and HH-S) are also identified towards the Pillar IV (see table 1 of Indebetouw et al. 2007). Healy, Hester & Claussen (2004) reported a water maser emission (see table 3 in their paper) towards the embedded source that is found between the red lobe [radial velocity range: (15, 50) km s^{-1}] and the blue lobe [radial velocity range: (−50, −15) km s^{-1}; see fig. 13 of Flagey et al. (2020)] investigated using the Hα radial velocity map. Linsky et al. (2007) did not detect X-ray emission towards the driving source; however, a weak X-ray source was found at the location of HH 216. Fig. 1(a) displays the dust continuum map at 850 μm, where the locations of Pillars I–IV and HH 216 are marked. Fig. 1(b) presents the *Spitzer* 4.5 μm image overlaid with the positions of HH-N, HH-S, bipolar structure (i.e. red and blue

lobes), and Pillar IV (see White et al. 1999; Flagey et al. 2020). The radio 8.71 GHz continuum emission contours are shown in Fig. 1(c), where the location of HH 216 is also indicated.

This paper focuses on studying the formation process of the driving source of the bow shock HH 216 and its internal structure, which are yet to be carried out. Furthermore, the nature of the radio emission associated with the HH 216 outflow (see Fig. 1a) is also examined using multifrequency data. Molecular line data are employed to study the distribution and kinematics of the molecular gas towards Pillar IV, which hosts the driving source of HH 216.

Section 2 presents various observational data sets used in this paper. The outcomes of this paper are presented in Section 3. Section 4 contains a thorough discussion of our observational findings. Finally, Section 5 gives the conclusions of the present work.

2 DATA SETS

We utilized observational data sets at different wavelengths (see Table 1) towards an area (size ∼3.82 × 6.14; central coordinates: $\alpha_{2000} = 18^h18^m55.39$ and $\delta_{2000} = −13°51'37.52$) highlighted by the dot–dashed box in Fig. 1(a).

The *HST* F657N image (Proposal ID: 13926; PI: Zolt Levay) was downloaded from the MAST archive. We obtained the level-3 science ready *JWST* NIRCam and MIRI images (Proposal ID: 2739; Proposal PI: Pontoppidan, Klaus M.) from the MAST archive. The

Table 1. Table provides information about the observational data sets used in this work.

Survey/facility	Wavelength/Frequency/line(s)	Resolution (arcsec)	Reference
NRAO VLA Archive Survey (NVAS)	4.89 GHz, 8.71 GHz	~1.55 and ~9.45	Crossley et al. (2007)
FOREST Unbiased Galactic plane Imaging survey with the Nobeyama 45-m telescope (FUGIN) survey	^{12}CO(J = 1−0), ^{13}CO(J = 1−0)	~20 and ~21	Umemoto et al. (2017)
James Clerk Maxwell Telescope (JCMT)	850 μm, CO(J = 3−2)	~14	PROJECT code = M16AP088; PI: Zhiyuan Ren
JWST ERO MIRI F770W, F1130W, F1500W imaging facility	7.7, 11.3, 15 μm	~0.44–0.70	Rieke et al. (2015), Wright et al. (2015)
Spitzer Galactic Legacy Infrared Mid-Plane Survey Extraordinaire (GLIMPSE)	3.6, 4.5, 5.8, 8.0 μm	~2	Benjamin et al. (2003), GLIMPSE Team (2020)
JWST ERO NIRCam Short Wavelength (SW) F090W, F187N, F200W imaging facility	0.901, 1.874, 1.99 μm	~0.07	Rieke, Kelly & Horner (2005), Beichman et al. (2012)
JWST ERO NIRCam Long Wavelength (LW) F335M, F444W, F470N imaging facility	3.365, 4.421, 4.707 μm	~0.17	Rieke, Kelly & Horner (2005), Beichman et al. (2012)
HST Wide Field Camera 3 (WFC3)/UVIS F657N imaging facility	6563 + 6583 Å	~0.067–0.156	Hester et al. (1996)

JWST facility had observed these images at broad, medium, and narrow-band filters. More details of *JWST* performance can be found in Rigby et al. (2023).

We examined the *Herschel* column density and dust temperature maps (resolution ~12″) in this work, which were generated for the *EU-funded ViaLactea project* (Molinari et al. 2010a) using the Bayesian Point Process Mapping (*PPMAP*) procedure (Marsh, Whitworth & Lomax 2015; Marsh et al. 2017) on the *Herschel* continuum images at 70–500 μm (Molinari et al. 2010b).

We also used the FUGIN ^{12}CO(J = 1 − 0) and ^{13}CO(J = 1 − 0) line data (plate scale = 8″.5 pixel^{-1}), which are calibrated in main beam temperature (T_{mb}, see Umemoto et al. 2017). According to Umemoto et al. (2017), the typical RMS noise levels (σ) for ^{12}CO and ^{13}CO lines are ~1.5 and ~0.7 K, respectively. The FUGIN line data have a velocity resolution of ~1.3 km s^{-1}. A Gaussian function with full-width at half maximum (FWHM) of 3 pixels (i.e. 25.5″) was used to smooth these data sets. Hence, the resultant angular resolution of these data sets is ~33″.

The processed James Clerk Maxwell Telescope's (JCMT's) ^{12}CO(J = 3–2) spectral data cube (rest frequency = 345.7959899 GHz) and the SCUBA-2 850 μm continuum map of the object 'g16' (proposal id: M16AP088) were downloaded from the JCMT Science Archive/Canadian Astronomy Data Centre (CADC). The JCMT line data are calibrated in antenna temperature (T_A). The line observations were obtained for an integration time of 1398 s, using the Heterodyne Array Receiver Programme/Auto-Correlation Spectral Imaging System (HARP; Buckle et al. 2009) spectral imaging system. The beam size, plate scale, and σ values for the data cube are ~14″, ~7″.3, and, ~1 K, respectively. The JCMT CO line data cube had a channel width of ~0.0265 km s^{-1}. Note that the JCMT line data are employed only for an area containing the object HH 216 and the Pillar IV.

3 RESULTS

3.1 Multiscale and multiwavelength view of HH 216

As mentioned earlier, Figs 1(a–c) highlight some previously known features/results towards M16, which are related to a bipolar outflow, an interesting object HH 216, HH-N, HH-S, and Pillars I–IV. We have also labelled a dense region as 'central dense structure' (hereafter 'CDS'), which is located between the base of Pillar II and the top of Pillar IV (see Fig. 1a). Note that this paper does not focus on the Pillars I–III and 'CDS'. The locations of the red lobe at V_{lsr} = [15, 50] km s^{-1} and the blue lobe at V_{lsr} = [−50, −15] km s^{-1} (from Flagey et al. 2020) are also marked in Fig. 1(b). The object HH 216 coincides with the red lobe and is also associated with the radio continuum emission at 8.71 GHz (see the ellipse in Fig. 1c).

The *Spitzer*-GLIMPSE images at 3.6–5.8 μm show a point-like source, G016.9105 + 00.7199 (at α_{2000} = $18^h18^m58^s.9$, and δ_{2000} = $-13°52'46''.97$) located close to HH-N (Figs 1b) and its photometric magnitudes are $m_{3.6}$ = 12.47 ± 0.23, $m_{4.5}$ = 11.19 ± 0.16, and $m_{5.8}$ = 9.93 ± 0.24 (see Spitzer Science 2009). This point-like object is the probable driving source of the outflow (see also Andersen et al. 2004; Indebetouw et al. 2007; Oliveira 2008; Flagey et al. 2020). Following the colour conditions [i.e. $(m_{4.5}-m_{5.8}) \geq 0.7$ and $(m_{3.6}-m_{4.5}) \geq 0.7$] reported in Hartmann et al. (2005) and Getman et al. (2007), this object is identified as a Class I protostar candidate. Considering these photometric magnitudes, we also carried out the spectral energy distribution of this particular object (see Indebetouw et al. 2007, for more details), favouring that it is a candidate low-mass object (~2–3 M$_\odot$).
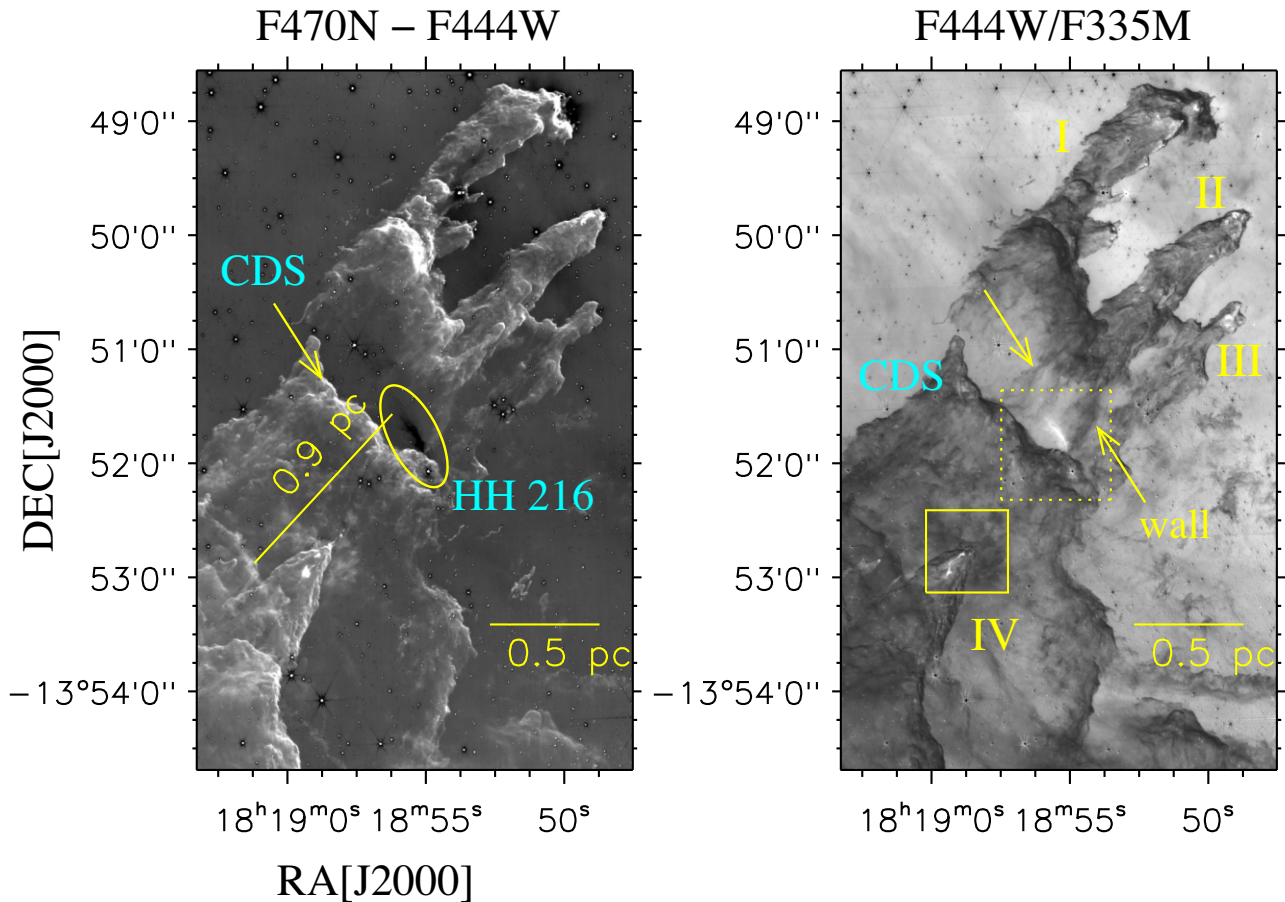
Figure 2. (a) *JWST* F470N−F444W (in linear scale; see the dot-dashed box in Fig. 1a). The ellipse shows the location of HH 216 as in Fig. 1(c). 'CDS' is also indicated by an arrow. (b) *JWST* F444W/F335M (in linear scale). The dotted box and the dot–dashed box encompass the area presented in Figs 3 and 6, respectively. Arrows highlight 'walls' of the Pillar II. In each panel, the *JWST* image is processed through median filtering with a width of 6 pixels and smoothing by 3 × 3 pixels using the 'box-car' algorithm. In all panels, a scale bar corresponding to 0.5 pc (at a distance of 1.74 kpc) is drawn.

In this paper, high-resolution *JWST* NIRCaM and MIRI images are examined to study the sub-structures towards HH 216 and Pillar IV. Previously, Reiter et al. (2022) examined the *JWST* F470N−F444W image to trace the H_2 emission at 4.693 μm in NGC 3324. Furthermore, Dewangan et al. (2017) employed the *Spitzer* ratio map of 4.5 μm/3.6 μm emission to study the signs of molecular outflows and the impact of massive stars on their surroundings in Sh 2-237. Nearly similar point response functions (PRFs) of the *Spitzer* 3.6 and 4.5 μm images allow them to create the *Spitzer* ratio map. We have also generated the F470N−F444W image and the ratio map of F444W and F335M using the *JWST* NIR images (see also Dewangan et al. 2023).

Fig. 2(a) displays the *JWST* F470N−F444W image, revealing the regions with the H_2 emission at 4.693 μm. The H_2 emission is evident towards HH-N and HH-S in Pillar IV. The object HH 216 is seen in the direction of the dark grey/black areas in Fig. 2(a). In Fig. 2(b), we present the *JWST* ratio map (i.e. F444W/F335M) of F444W ($\lambda_{eff}/\Delta\lambda$: 4.421/1.024 μm) and F335M ($\lambda_{eff}/\Delta\lambda$: 3.365/0.347 μm) images, indicating the presence of the 3.3 μm polycyclic aromatic hydrocarbon (PAH) feature (see dark grey/black areas). Here, one can note that the *JWST* NIRCam F444W filter lacks the 3.3 μm PAH feature. The areas with the noticeable 4.05 μm Brα feature and/or the 4.693 μm H_2 emission seem to be identified by the bright areas in the *JWST* ratio map. The regions with the 4.05 μm Brα emission

in the *JWST* ratio map can be easily found by looking at the locations with the 4.693 μm H_2 emission seen in the *JWST* F470N−F444W image. On the basis of this approach, the Brα emission is traced towards the object HH 216, HH-N, and HH-S. The 3.3 μm PAH feature is seen towards 'CDS' and outer boundaries/walls of Pillars I–IV. Additionally, the boundaries/walls of Pillar II may also be seen extending in the southern direction, where one end of HH 216 appears to connect to one of the boundaries/walls of Pillar II (see Fig. 2b).

Using the *JWST* NIR & MIR, *HST* F658N, and NVAS radio continuum images, a small area hosting HH 216 is presented in Figs 3(a)–(g). The NVAS radio 8.71 GHz continuum emission contours (rms ∼1.84 mJy beam^{-1}) are overlaid on the F1130W image (see Fig. 3f), while the F1500W image is overlaid with the NVAS radio 4.89 GHz continuum emission contours (rms ∼60.2 μJy beam^{-1}; see Fig. 3g). For a comparison purpose, the *JWST* F470N−F444W and F444W/F335M images are also shown in Figs 3(h and i), respectively. In Figs 3(b and i), arrows indicate the Pillar II's wall/boundary and HH 216. The object HH 216 is associated with the ionized emission as traced in the radio continuum maps, *JWST* ratio map, and *HST* F658N image. These data sets also suggest the presence of sub-structures in HH 216.

In order to infer the nature of radio continuum emission associated with the object HH 216, we have computed a radio spectral index (α) map using the NVAS maps at 4.89 and 8.71 GHz. In general, a
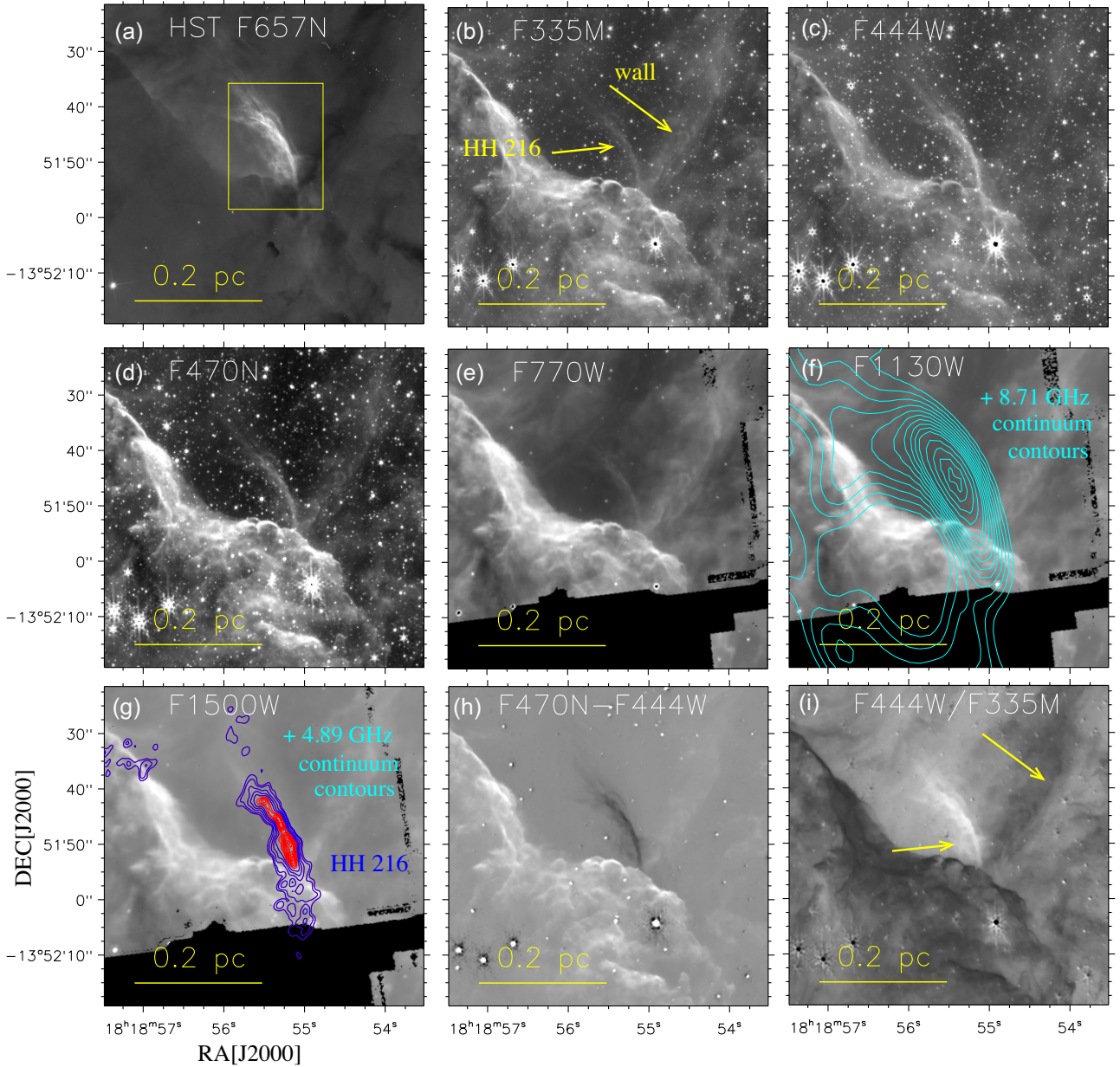
Figure 3. Multiwavelength view of the area hosting HH 216 (see the dotted box in Fig. 2b). a) *HST* F657N image. The dot-dashed box encompasses the area presented in Figs 5(a–c). (b–g) *JWST* F335M, F444W, F470N, F770W, F1130W, and F1500W images are displayed, respectively. (h) F470N−F444W (in linear scale). (i) F444W/F335M (in linear scale). In panel 'f', the 8.71 GHz radio continuum emission contours (in cyan) are also shown and the contour levels are 17.22 mJy beam^{-1} × (0.15, 0.2, 0.25, 0.3, 0.35, 0.4, 0.45, 0.5, 0.55, 0.6, 0.7, 0.8, 0.9, and 0.98). In panel 'g,' the 4.89 GHz radio continuum emission contours (in blue and red) are also overlaid on the *JWST* F1500W image. The blue contours are shown with the levels of 1.23 mJy beam^{-1} × (0.15, 0.2, 0.3, 0.4, and 0.5), while the red contours are presented with the levels of 1.23 mJy beam^{-1} × (0.6, 0.65, 0.7, 0.75, 0.8, 0.85, 0.9, 0.95, and 0.98). In each panel, a scale bar corresponding to 0.2 pc (at a distance of 1.74 kpc) is drawn.

relation, $F_\nu \propto \nu^\alpha$, is known, where ν is the frequency of observation and F_ν is the corresponding observed flux density. A positive spectral index (i.e. $\alpha > 0$) indicates that the emission has a thermal origin, whereas a negative spectral index (i.e. $\alpha < 0$) shows the presence of non-thermal emission (e.g. Rybicki & Lightman 1979; Longair 1992). In this relation, first, the radio map at 4.89 GHz (beam size $\sim 1\rlap{.}{''}85 \times 1\rlap{.}{''}26$ or $\sim 1\rlap{.}{''}55$) was convolved to the beam size of the radio map at 8.71 GHz (i.e. $11\rlap{.}{''}84 \times 7\rlap{.}{''}07$ or $\sim 9\rlap{.}{''}45$) using the CASA 'imsmooth' task, and was also regridded to the pixel size of the radio map at 8.71 GHz ($\sim 1\rlap{.}{''}82$) using the IDL function 'hastrom'.

In Fig. 4(a), we have overlaid the 4.89 GHz radio continuum emission contours on the radio continuum map at 8.71 GHz. Using the total fluxes at 4.89 and 8.71 GHz of HH 216, we have computed an average value of the spectral index to be 0.33 ± 0.15.

Furthermore, we employed a pixel-wise fitting approach for the flux densities from these two radio maps, resulting in a radio spectral index map (see Fig. 4b). In the direction of HH 216, a variation in the spectral index can be observed, ranging from -0.74 to 1.45. This variation represents a smooth gradient from negative to positive values as we move towards the northeast direction. This finding
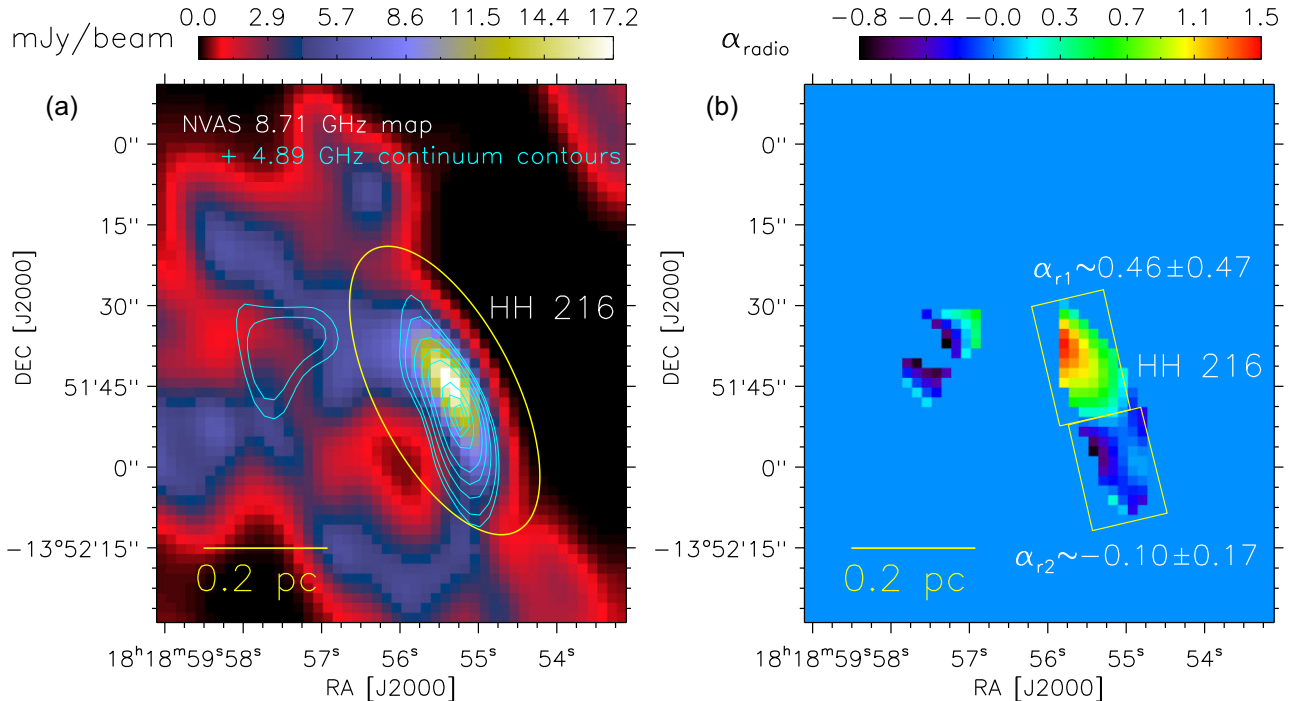
Figure 4. (a) Overlay of the NVAS 4.89 GHz radio continuum contours on the 8.71 GHz radio continuum map in the direction of HH 216. The beam size of both the radio maps is $\sim 11\overset{''}{.}84 \times 7\overset{''}{.}07$ (or $\sim 9\overset{''}{.}45$). The cyan contours are shown with the levels of 12.9 mJy beam^{-1} × (0.25, 0.3, 0.4, 0.5, 0.6, 0.8, and 0.95). The ellipse indicates the location of HH 216. (b) Radio spectral index map (resolution $\sim 11\overset{''}{.}84 \times 7\overset{''}{.}07$) of M16 produced for pixels above the 3σ level in the 4.89 and 8.71 GHz bands. In the direction of HH 216, two small boxes are plotted, and an average value of the spectral index for each box is also indicated in the panel. In each panel, a scale bar corresponding to 0.2 pc (at a distance of 1.74 kpc) is drawn.

allows us to select two small areas/boxes (i.e. 'r1' and 'r2'; see Fig. 4b) towards HH 216. The mean spectral index values are determined to be 0.46 ± 0.47 and -0.10 ± 0.17 for the top box (i.e. 'r1') and the bottom box (i.e. 'r2'), respectively. This exercise seems to suggest the presence of a mix of both thermal and non-thermal radio emission towards HH 216. It is noted that the area 'r2' having a negative spectral index is located towards the Pillar II's wall/boundary. Further exploration of the non-thermal radio emission towards HH 216, low-frequency radio continuum observations (i.e. below 800 MHz) will be helpful.

To study sub-structures, a zoomed-in view of the object HH 216 is presented in Figs 5(a and b). Fig. 5(a) displays the *HST* F657N image. The NVAS 4.89 GHz continuum emission map (beam size $\sim 1\overset{''}{.}55$) and contours is presented in Fig. 5(b). Several ionized or radio continuum peaks are seen towards HH 216. From Fig. 5(a), we find at least two sub-structures (below 3000 au) associated with ionized emission towards HH 216, which appear to be intertwined/entangled. Such configuration or entangled sub-structures may be also seen in the *JWST* F470N−F444W image (see Fig. 3h) and the *JWST* F444W/F335M image (see Fig. 3i).

As highlighted earlier, Pillar IV hosts HH-N, HH-S, and the driving source of the bipolar outflow. To examine the embedded environment of Pillar IV, using the *JWST* images, a zoomed-in view is displayed in Fig. 6. The *JWST* F335M, F444W, F470N, F470N−F444W, and F444W/F335M images are shown in Figs 6(a–e), respectively. Fig. 6(f) presents a two colour composite image using the F444W/F335M (in red) and F470N−F444W (in turquoise) images. The *JWST* images at $\lambda \geq 2\,\mu$m have revealed the driving source of the bipolar outflow ($\alpha_{2000} = 18^h 18^m 58\overset{s}{.}8$; $\delta_{2000} = -13°52'47\overset{''}{.}7$), which is at an offset of $1\overset{''}{.}5$ from the position of the *Spitzer* source,

G016.9105 + 00.7199. The locations of HH-N, HH-S, and the powering source, are indicated in each panel of Fig. 6. Using the *JWST* MIR RGB map (F1500W (in red), F1130W (in green), and F770W (in blue) images), in Fig. 6(b), the inset shows a zoomed-in view to an area hosting the driving source. This source is saturated in the *JWST* F444W and F770W images and appears as a single object (below 1000 au) in the *JWST* images. The H$_2$ emission at 4.693 µm is traced towards HH-N, HH-S, and the tip of the Pillar IV (see Figs 6c and d). Apart from the objects HH-N and HH-S, we have also highlighted three new H$_2$ features in Fig. 6(d), which are HH-Na, HH-Nb, and HH-Nc. A separation between the driving source and the object HH-Nc is ~ 0.13 pc (see Fig. 6f). We determine that the sky-projected distance between HH-Na and HH-Nb is ~ 13789.5 au, but the separation between HH-Nb and HH-Nc is ~ 6264 au. The boundaries of Pillar IV are clearly depicted in the H$_2$ and PAH emission (see Figs 6d and e). In Figs 6(e and f), the 4.05 µm Brα emission is also detected towards both HH-N and HH-S, but no 4.05 µm Brα emission is found towards the tip of the Pillar IV (see HH-Na, HH-Nb, and HH-Nc). Interestingly, an elongated feature (extent ~ 0.16 pc) containing HH-N and HH-S at its opposite edges, is also traced with the Brα emission (see a cyan contour in Fig. 6e). This could be one part of the ionized jet, which is located on the southern side of the driving source.

3.2 Kinematics of molecular gas

3.2.1 FUGIN molecular line data

This section deals with the study of molecular line data towards Pillar IV and its surroundings in M16. We employed the FUGIN ^{12}CO($J = 1$–0) and ^{13}CO($J = 1$–0) line data, and the molecular
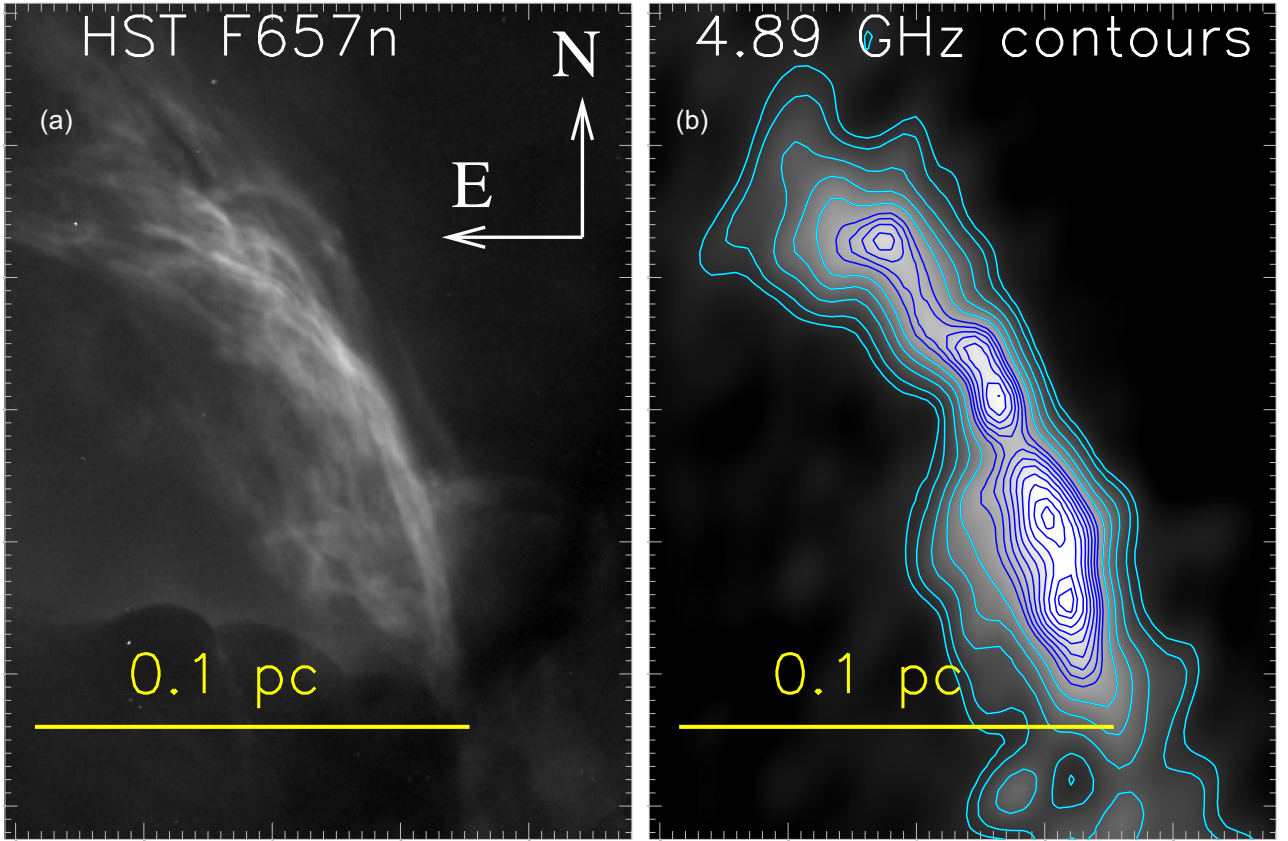
Figure 5. A zoomed-in view of HH 216 using the multiwavelength images (see the dot–dashed box in Fig. 3a). (a) *HST* F657N image. (b) NVAS 4.89 GHz radio continuum emission map (beam size $\sim 1''.55$) and contours. Contours (in cyan and blue) are the same as presented in Fig. 3(g). In each panel, a scale bar corresponding to 0.1 pc (at a distance of 1.74 kpc) is plotted.

emission is studied in a velocity range of [19.275, 27.725] km s^{-1}. To study the distribution of molecular gas, the integrated intensity map, the line-of-sight intensity weighted velocity map, and the position-velocity diagram are produced using the molecular (i.e. ^{12}CO(J = 1–0) and ^{13}CO(J = 1–0)) line data. Integrated intensity maps of ^{12}CO(J = 1–0) and ^{13}CO(J = 1–0) are presented in Figs 7(a and b), respectively. Molecular gas is traced towards the previously known Pillars I–IV and 'CDS'. Figs 7(c and d) show intensity weighted velocity maps of ^{12}CO(J = 1–0) and ^{13}CO(J = 1–0), respectively. Both the intensity weighted velocity maps hint at the presence of two velocity components towards M16.

Figs 7(e and f) present position (or right ascension)-velocity diagrams of ^{12}CO(J = 1–0) and ^{13}CO(J = 1–0), respectively, which reveal two velocity components around 23 and 26 km s^{-1} and their connections in velocity. To produce this position-velocity diagram, we integrated the molecular emission over the declination range from -13.935 to -13.803 degrees. On the basis of the position-velocity diagrams, we have selected velocity ranges of two cloud components, which are [19.275, 23.825] and [24.475, 27.725] km s^{-1}. Using the ^{12}CO(J = 1–0) and ^{13}CO(J = 1–0) line data, the spatial distribution of these two cloud components and their overlapping areas is examined (not shown here). Using the ^{13}CO(J = 1–0) emission, the cloud components at [24.475, 27.725] and [19.275, 23.825] km s^{-1} are presented in Figs 8(a and b), respectively. In Figs 8(a and b), the background is the JCMT 850 μm continuum map as presented in Fig. 1(a). The Pillar IV is associated with the blue-shifted cloud at [19.275, 23.825] km s^{-1} (see Fig. 8b), which

seems to be spatially located towards the intensity-depression region in the red-shifted cloud at [24.475, 27.725] km s^{-1} (see an arrow in Fig. 8a). Such configuration shows a complementary distribution of the two cloud components towards the Pillar IV, which can be considered as an interesting finding. Additionally, we find that the molecular gas associated with the blue-shifted cloud component is also seen towards the Pillars II and III (see Fig. 8b). These outcomes are also found in the ^{12}CO(J = 1–0) emission (not shown here).

Fig. 8(c) displays the *Herschel* column density (N(H$_2$)) map, showing the presence of high values (1–3.6 $\times$ 10^{22} cm^{-2}) towards Pillar IV. In the direction of Pillar IV, a contour with N(H$_2$) = 1.3 $\times$ 10^{22} cm^{-2} is also plotted in Fig. 8(c; see also Fig. 8d). Following the analysis presented in Dewangan et al. (2020), the *Herschel* column density map enables us to compute the total mass of Pillar IV to be $\sim$36 M$_\odot$. In Fig. 8(d), we present the *Herschel* dust temperature (T_d) map. The Pillar IV is found with $T_d \sim$24 K and is surrounded by warm dust emission ($T_d \sim$25–27 K; see the white contour in Fig. 8d).

3.2.2 JCMT molecular line data

To further study the cloud components towards Pillar IV, we have also examined the JCMT CO(J = 3–2) line data at [20.514, 29.404] km s^{-1}, which have better resolution compared to the FUGIN line data. Figs 9(a and b) display the integrated intensity and intensity weighted velocity maps of the JCMT line data, respectively. In Figs 9(c),
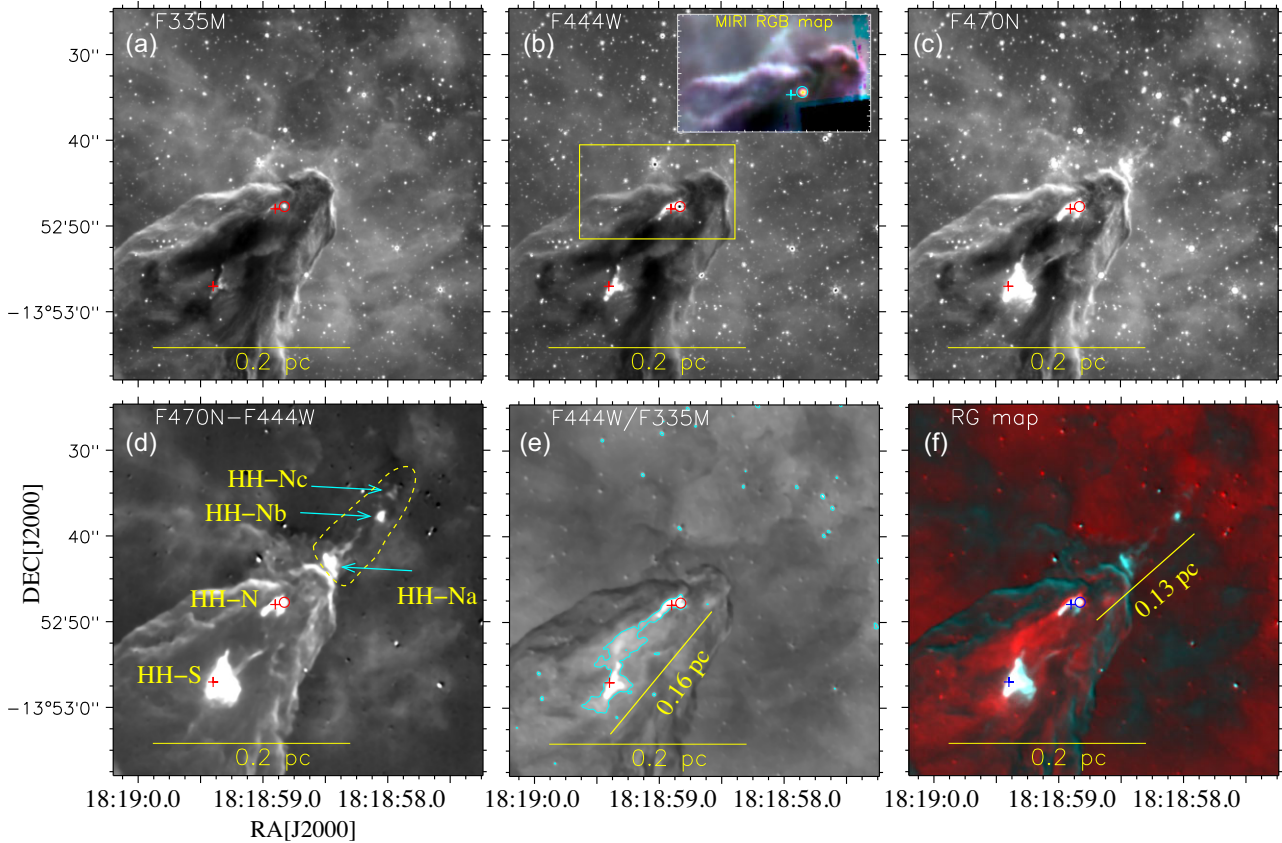
Figure 6. A zoomed-in view of Pillar IV using the multiwavelength images (see the dot–dashed box in Fig. 2b). (a) *JWST* F335M image. (b) *JWST* F444W image. An inset on the top right presents a zoomed-in view of the central region (see the dot–dashed box in Fig. 6b). The inset is a three-colour composite map made using the F1500W (in red), F1130W (in green), and F770W (in blue) images. (c) *JWST* F470N image. (d) F470N−F444W image (in linear scale). Some noticeable H$_2$ knots are also labelled and highlighted in the panel. (e) F444W/F335M image (in linear scale). A contour (in cyan) highlights an elongated emission feature traced in the F444W/F335M image. (f) A two-color composite map made using F444W/F335M (in red) and F470N−F444W (in turquoise). In each panel, cross symbols are the same as shown in Fig. 1(b), and the circle represents the location of the driving source of the previously reported outflow. In all panels, a scale bar corresponding to 0.2 pc (at a distance of 1.74 kpc) is plotted.

we show the position (or right ascension)-velocity diagram of the ^{12}CO(J = 3–2) emission. For the position-velocity diagram, the molecular gas is integrated over the declination range from −13.935 to −13.835 degrees. Interestingly, the JCMT line data also support the presence of two cloud components (at [25.49, 29.40] and [20.51, 25.01] km s^{-1}) towards the Pillar IV and 'CDS'. Fig. 9(d) presents a two-colour composite image made using the ^{12}CO(J = 3–2) map at [25.49, 29.40] km s^{-1} (in red) and at [20.51, 25.01] km s^{-1} (in turquoise), allowing us to examine the spatial distribution of these cloud components. In the direction of the Pillar IV and 'CDS', overlapping areas of the two cloud components are seen in white colour (see Fig. 9d). To further explore these findings, more analysis of the molecular gas is presented in Figs 10–12.

Fig. 10 presents the JCMT CO(J = 3–2) channel maps from 19 to 30 km s^{-1} with a velocity interval of 0.92 km s^{-1}. On the basis of a visual appearance, we have marked an arbitrary curve in each panel of Fig. 10, which seems to highlight the location of the Pillar IV (see also Figs 9b). From Fig. 10, we can examine the molecular gas associated with the two cloud components (see Figs 10 c–f and g–k). In Figs 10(g and h), we can find the common zones of the two cloud components. In Fig. 11, we display the spectra of the JCMT CO(J = 3–2) emission towards nine circular regions (s1–s9) marked in Fig. 9(a). In the direction of the circular regions s4 and s6, two velocity peaks are found. We can compare the peak velocities

towards the circular regions 's1–s3' (around 26 km s^{-1}) with the peak velocities in the direction of the circular regions s5, s7, s8, and s9 (around 23 km s^{-1}). The study of the spectra supports the presence of two cloud components towards the Pillar IV. Figs 12(a)–(i) show position-velocity diagrams of the JCMT CO(J = 3–2) emission along nine arrows (see Fig. 9c), while in Fig. 12(j), we display the position-velocity diagram along a curve 'YZ' (see Fig. 9c). It should be noted that this curve is chosen in the direction of Pillar IV's length, and the arrows are selected perpendicular to Pillar IV. In this direction of the Pillar IV, these diagrams suggest the existence of two cloud components and their connection (see Figs 12 a–e and j). In particular, a feature at the intermediate velocity range (i.e. [25.04, 25.46] km s^{-1}) is also seen between the two cloud components around 23 and 26 km s^{-1} (see Fig. 12j).

Using the JCMT CO(J = 3–2) line data, the integrated intensity map [at (25.04, 25.46) km s^{-1}] towards Pillar IV is presented in Fig. 13(a). The selected area in Fig. 13(a) is highlighted by the dot–dashed box in Fig. 9(d). The molecular emission traced in the intermediate velocity range is seen towards the inner parts of the Pillar IV. The *JWST* F470N image is overlaid with the two cloud components traced in the JCMT CO(J = 3–2) line data towards Pillar IV (see Fig. 13b). The driving source of the outflow seems to be located towards the common zones of the two cloud components (see the circle in Fig. 13b).
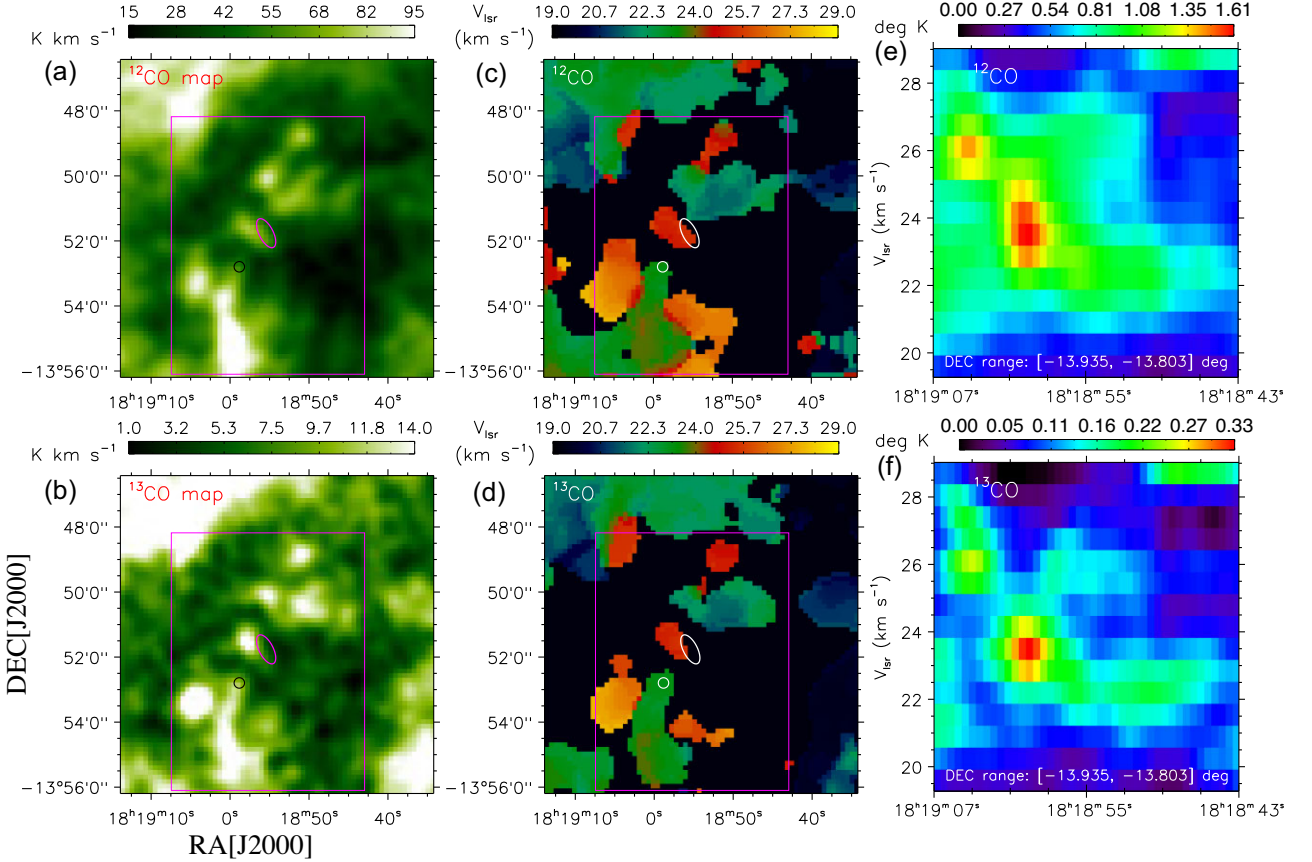
Figure 7. (a) FUGIN ^{12}CO($J = 1$–0) integrated intensity map (at [19.275, 27.725] km s^{-1}). (b) FUGIN ^{13}CO($J = 1$–0) integrated intensity map. (c) The line-of-sight intensity weighted velocity map of the FUGIN ^{12}CO($J = 1$–0) emission. (d) FUGIN ^{13}CO($J = 1$–0) intensity weighted velocity map. (e) Position (or right ascension)-velocity diagram of the FUGIN ^{12}CO($J = 1$–0) emission. The molecular emission is integrated over the declination range from -13.935 degrees (or $-13°56'06''.0$) to -13.803 degrees (or $-13°48'10''.8$) degrees (see a solid box in Figs 7 a–d). (f) Same as Fig. 7(e), but for the FUGIN ^{13}CO($J = 1$–0) emission. In panels 'a–d', the circle represents the location of the driving source of the previously reported outflow (see Fig. 6), and the ellipse shows the location of HH 216. The selected area in panels 'a–d' is the same as presented in Fig. 1(a). A solid box highlights an area containing major structures in M16 (see panels 'a–d').

We have discussed the implication of these outcomes in more detail in Section 4.

4 DISCUSSION

The M16 H II region is an extended star-forming site (∼10 pc) and is associated with the most famous astronomical object in the sky, Pillars of Creation (see Pillars I–IV in Fig. 1a). Previous works suggested that the Pillars's direction and structure are influenced by the molecular cloud's pre-existing structure, which is shaped by the radiation field of the nearby massive stars (see Karim et al. 2023; Lei et al. 2023, and references therein). Embedded protostars have been investigated towards the tips of these Pillars, where significant [C II] line and PAH emissions have been detected (Karim et al. 2023, see also the *JWST* F444W/F335M map in Fig. 2b). To explain the origin of these Pillars, Lei et al. (2023) discussed three models, which are the instability model, cometary model, and shielding model (see their paper for more details). According to these authors, many numerical simulations have been conducted using the shielding model, which has drawn more interest in recent years. A detailed study of the Pillars' kinematic structure is presented in Karim et al. (2023). Note that the present work mainly focuses on the Pillar IV (including HH 216) and the implication of the presence of molecular cloud components towards the Pillar IV.

4.1 Multiscale picture of ionized knot HH 216 and Pillar IV

The ionized knot, HH 216, has been considered as the bow shock of a bipolar jet (Meaburn & White 1982; Meaburn & Whitehead 1990; Andersen et al. 2004; Flagey et al. 2020) and is traced at radial velocities up to 150 km s^{-1} in the [O III]λ5007 line (see Meaburn & Whitehead 1990). HH 216 is associated with the red-shifted outflow lobe, which is seen away from the Pillar IV, while the blue-shifted outflow lobe and its driving source are traced in Pillar IV. According to Flagey et al. (2020), the total extent of the bipolar geometry is ∼1.8 pc (at a distance of 2.0 kpc). Andersen et al. (2004) discussed the inclination of the HH flow to be at least 36 degrees with respect to the plane of the sky. The *JWST* NIR and MIR images have resolved the position of the Class I protostar that drives a bipolar outflow and is embedded in Pillar IV (see Section 3.1). The *JWST* images do not detect any H$_2$ emission towards HH 216; however, the Brα emission and the radio continuum emission are traced towards this object. Anglada, Rodríguez & Carrasco-González (2018) highlighted the measured centimetre radio luminosity (i.e. S$_ν$d^2) values range from ∼100 mJy kpc^2 for massive young stars to ∼3 × 10^{-3} mJy kpc^2 for young brown dwarfs. Using the NVAS 4.89 GHz continuum emission towards HH 216 (see Fig. 3g), we have computed the total flux (S$_ν$) of ∼22.96 mJy (size ∼13''.4 × 30''.2) within the contour level of 0.227 mJy beam^{-1} (rms ∼60.2 μJy beam^{-1}), which allows us to determine

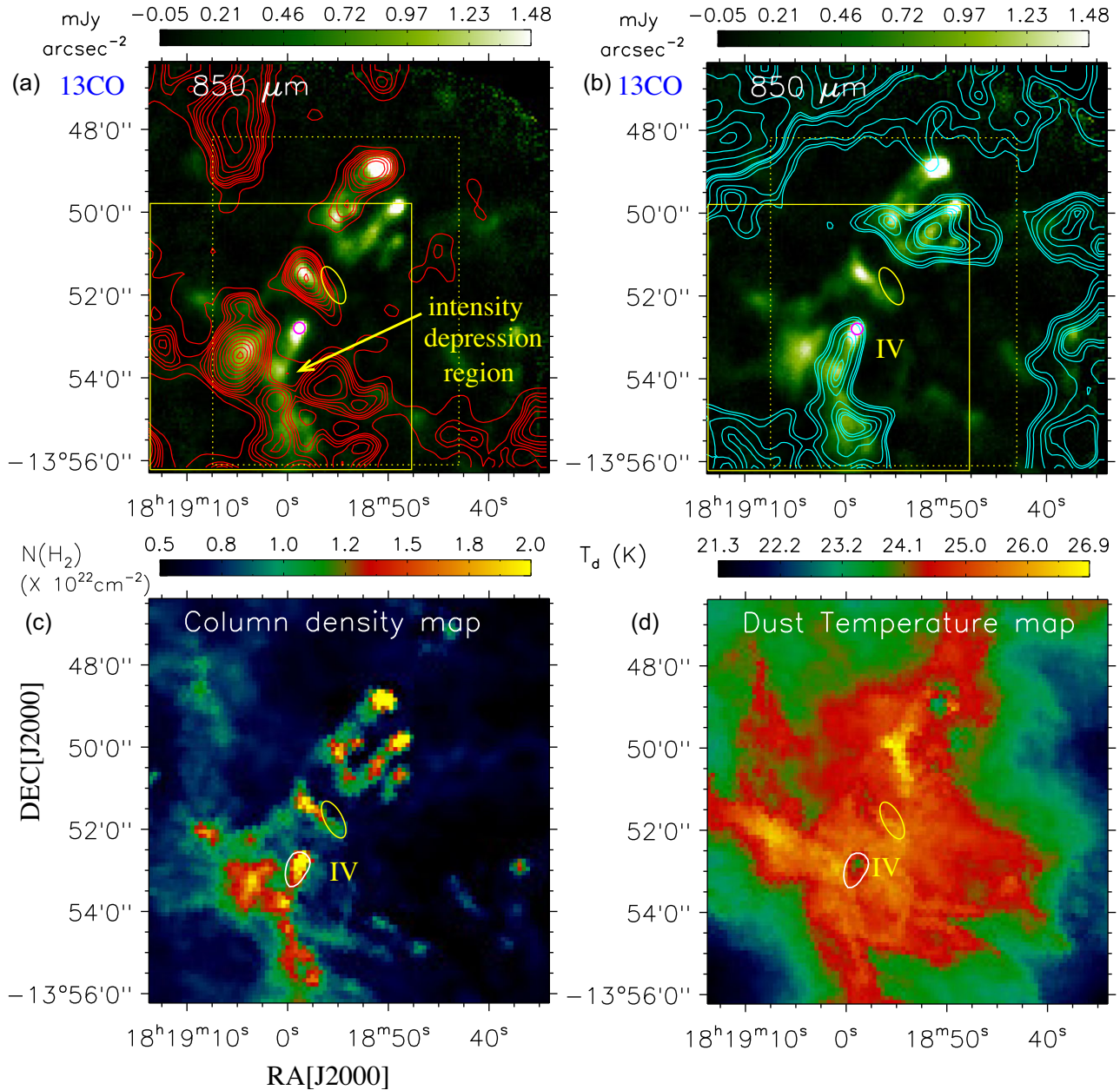**Figure 8.** (a) Overlay of the ^{13}CO(J = 1–0) emission contours (in red; at [24.475, 27.725] km s^{-1}) on the 850 μm continuum emission map. The contours are 18.01 K km s^{-1} × (0.15, 0.2, 0.22, 0.24, 0.27, 0.3, 0.35, 0.4, 0.5, 0.6, 0.7, 0.8, 0.9, and 0.98). (b) Overlay of the ^{13}CO(J = 1–0) emission contours (in cyan; at [19.275, 23.825] km s^{-1}) on the 850 μm continuum emission map. The contours are 17.76 K km s^{-1} × (0.32, 0.35, 0.4, 0.5, 0.55, 0.58, 0.6, 0.7, 0.8, 0.9, and 0.98). (c) *Herschel* column density map. (d) *Herschel* dust temperature map. In panels 'a' and 'b', boxes highlight areas containing major structures in M16. In panels 'c' and 'd', a contour (in white) with $N(\mathrm{H_2}) = 1.3 \times 10^{22}$ cm^{-2} is also shown.

the observed centimetre radio luminosity (i.e. $S_\nu d^2$ (in mJy kpc^2)) to be ~69.5 mJy kpc^2 at a distance (*d*) of 1.74 kpc.

It is thought that the interaction of shocks in the associated jet with the surrounding molecular cloud may increase the temperature and density of the gas, which may dissociate H$_2$, and H may start to be ionized (e.g. Anglada et al. 2018). Hence, shocks in the jet may be responsible for the ionizing process of the radio jet or the ionized knot HH 216.

The analysis of the NVAS radio 4.89 and 8.71 GHz continuum maps favours the presence of thermal and non-thermal radio emission towards HH 216 (see Fig. 4 and Section 3.1). New low-frequency

radio continuum observations are needed to further confirm the non-thermal radio emission. If there exists non-thermal radio emission in HH 216, then such areas seem to be located towards its southern end, which may be linked with the wall of Pillar II (see Section 3.1). Such an area may be targeted for probing the physical mechanisms responsible for particle acceleration (e.g. Padovani et al. 2015, 2016).

The *JWST* and *HST* images reveal entangled ionized structures (below 3000 au) towards the bow shock of HH 216 (see Fig. 5c), which may be located towards termination shocks. The observed entangled structures, where at least four ionized peaks are detected
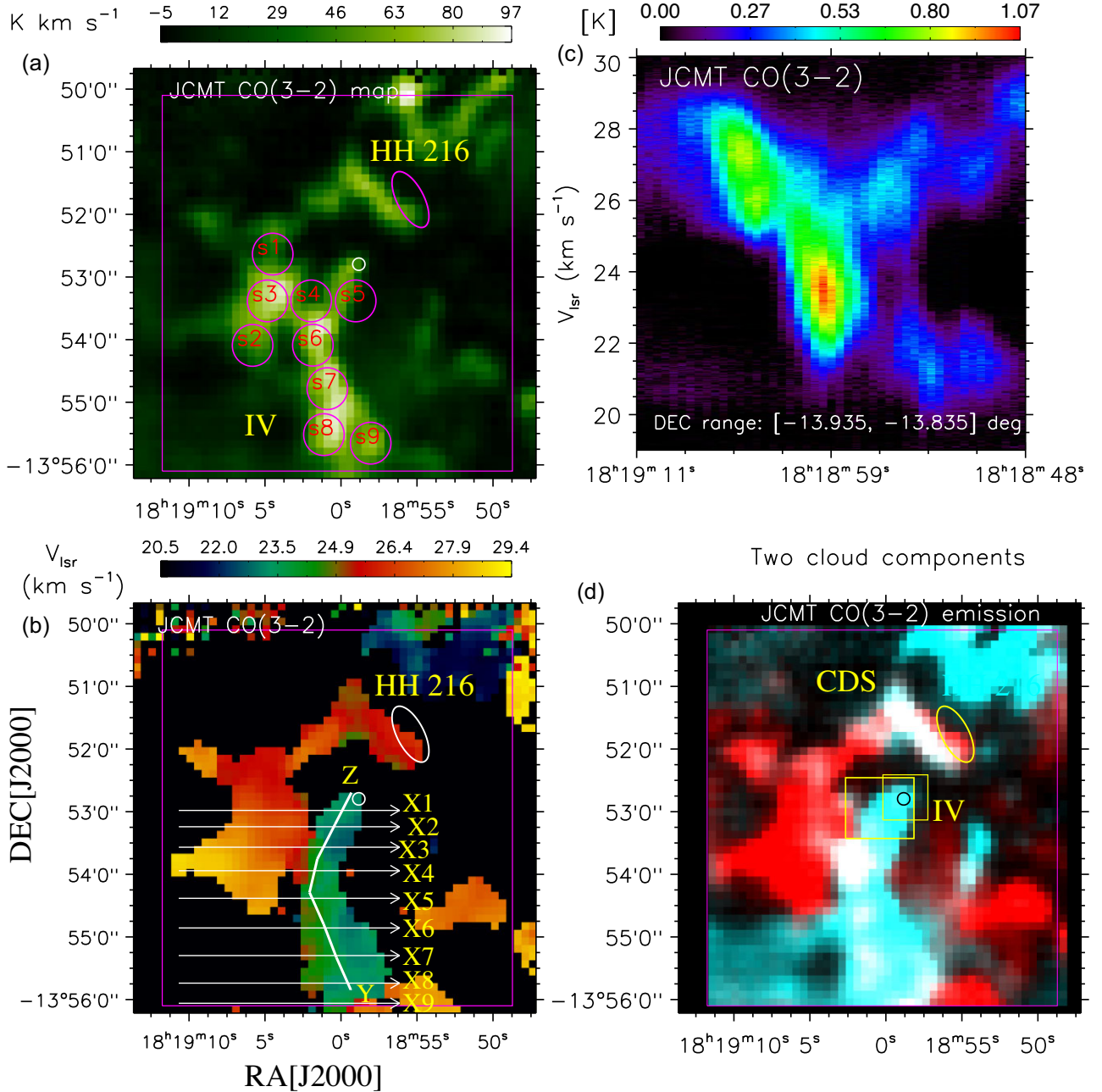
Figure 9. (a) JCMT CO(J = 3–2) integrated intensity map (at (20.514, 29.404) km s^{-1}] of an area hosting mainly the object HH 216 and the Pillar IV (see the dot–dashed box in Fig. 8b). Nine circular regions (i.e. s1–s9; radii = 20 arcsec) are indicated, where mean velocity profiles are produced (see Fig. 11). (b) JCMT CO(J = 3–2) intensity weighted velocity map. Nine arrows 'X1–X9' and one curve 'YZ' are marked in the panel, where the position-velocity diagrams are produced (see Fig. 12). (c) Position (or right ascension)-velocity diagram of the CO(J = 3–2) emission. The molecular emission is integrated over the declination range from −13.935 degrees (or −13°56′06″.0) to −13.835 degrees (or −13°50′06″.0) (see a solid box in Fig. 9a). (d) Spatial distribution of the JCMT CO(J = 3–2) gas associated with the two clouds at [25.49, 29.40] km s^{-1} (in red) and [20.51, 25.01] km s^{-1} (in turquoise). The dot–dashed box shows the area presented in Fig. 13(a), while the small solid box displays the area shown in Fig. 13(b). In panels 'a', 'b', and 'd', symbols are the same as shown in Fig. 8(a).

in the NVAS radio 4.89 GHz continuum map, could be resultant from the interaction of shocks in the jet with its environment. This interaction may be responsible for compression, heating, and variations of the magnetic field strength (and/or direction) towards HH 216 (e.g. Anglada et al. 2018). Modelling of the entangled ionized structures will be helpful, and is beyond the scope of this work.

The *JWST* images reveal new knots (i.e. HH-Na, HH-Nb, and HH-Nc) in the H$_2$ emission, which are located towards the northern side of Pillar IV (see Fig. 6d). We do not find any Brα emission towards these knots. These observed H$_2$ knots support the picture of episodic accretion in the powering source of HH 216 as previously reported by Flagey et al. (2020). An ionized feature (i.e. one of the parts of the jet; extent ∼0.16 pc) is investigated in the southern side of
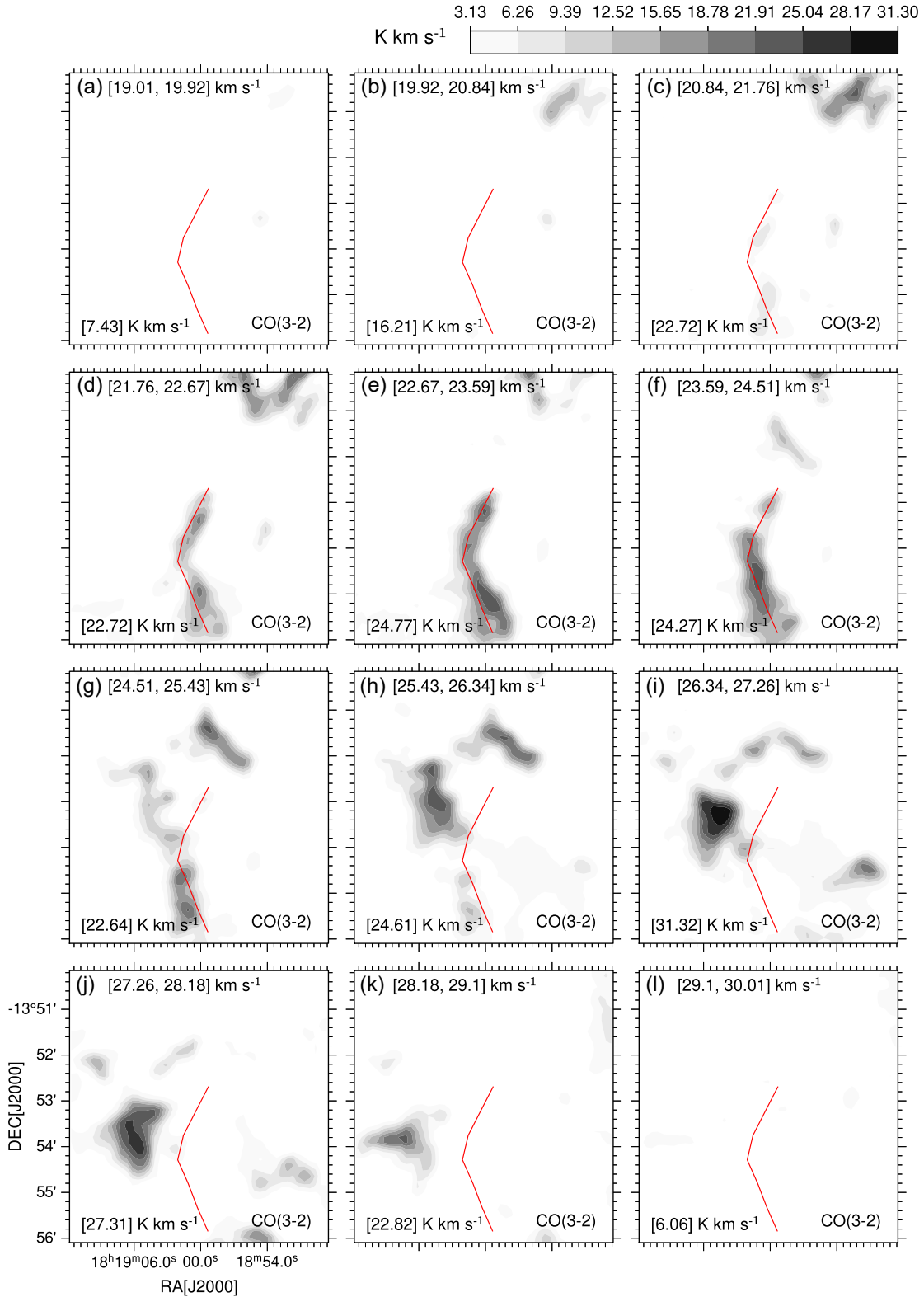
Figure 10. JCMT CO($J = 3$–2) channel maps from 19 to 30 km s^{-1} with a velocity interval of 0.92 km s^{-1}. The curve (in red) is the same as shown in Fig. 9(b).

the protostar embedded in the central part of Pillar IV. This ionized feature seems to be associated with the blue-shifted lobe. We note that the NVAS radio continuum maps do not cover the area hosting Pillar IV. Therefore, we are unable to further explore this ionized jet in this work. In the direction of the driving source, we do not find any other point source within a scale of 1000 au in the *JWST* images. It implies that a single source is responsible for the outflow or the episodic bursts.
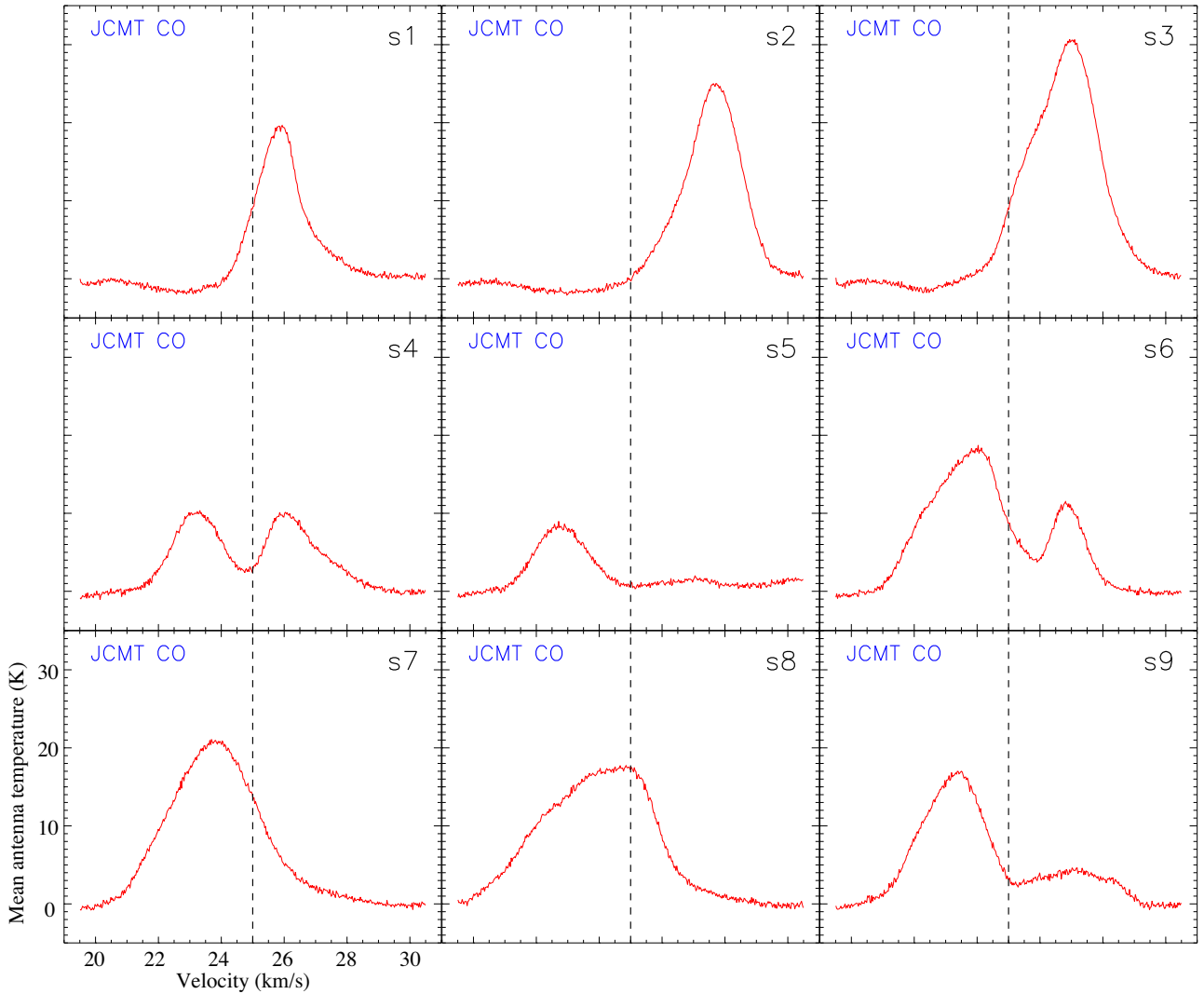
Figure 11. JCMT CO($J = 3\text{–}2$) spectra towards nine circular regions (i.e. s1–s9) marked in Fig. 9(a). In each panel, the dashed line at $V_{lsr} = 25$ km s^{-1} is highlighted.

Overall, the applicability of a jet/bow shock mechanism is possible as previously suggested by Meaburn & Whitehead (1990; see also Flagey et al. 2020).

4.2 Signatures of cloud-cloud collision towards Pillar IV

Previously, bulk velocities around 26 and 22.5 km s^{-1} were reported towards the peaks of Pillar I and Pillar II/III in M16, respectively (Pound 1998; White et al. 1999; Tremblin et al. 2013), suggesting the presence of different velocity components. In the direction of Pillars I, II, and III, Karim et al. (2023) presented the position-velocity diagrams of CO (see figs 8 and 9 in their paper). However, these authors did not explore any position-velocity diagrams towards the Pillar IV. Hence, there has not been done a thorough analysis of molecular line data towards Pillar IV. In a wide spatial scale, using the NANTEN2 and FUGIN ^{12}CO line data, Nishimura et al. (2021) identified two velocity components in the direction of the giant molecular cloud (GMC) associated with M16 (size ~10 pc × 30 pc), which are 9.2–19.6 km s^{-1} (i.e. blue-shifted component) and 24.2–31.3 km s^{-1} (i.e. red-shifted component). They suggested that the GMC endured numerous collision events [or cloud-cloud collision (CCC)] over the course of several 10^6 yr. They also claimed that the older collision event accounts for the presence of O-type stars in the NGC 6611 cluster in M16. The age of M16 is reported to be 1.3 ± 0.3 Myr (Bonatto, Santos & Bica 2006).

It has been proposed that supersonic collision between molecular clouds produces a shock-compressed interface with amplified magnetic field (e.g. Habe & Ohta 1992; Anathpindika 2010; Inoue & Fukui 2013; Haworth et al. 2015a, b; Balfour, Whitworth & Hubber 2017; Torii et al. 2017; Bisbas et al. 2017, and references therein), where massive stars and clusters of YSOs can be formed. In favour of the proposed collision event, we find several observational works in the literature (e.g. Torii et al. 2011, 2015, 2017; Fukui et al. 2014, 2018, 2021; Dhanya et al. 2021; Maity et al. 2022, 2023). In the collision event, we expect at least two cloud components and their connection in both spatial and velocity space. In such process, a bridge feature, which is a low-intensity feature connecting two cloud components with an intermediate velocity range in position-velocity diagrams, is anticipated (e.g. Haworth et al. 2015b; Dewangan & Ojha 2017; Kohno et al. 2018; Dewangan et al. 2018a; Priestley & Whitworth 2021). The bridge feature has been suggested to hint the presence of the turbulent motion of the gas enhanced by the collision
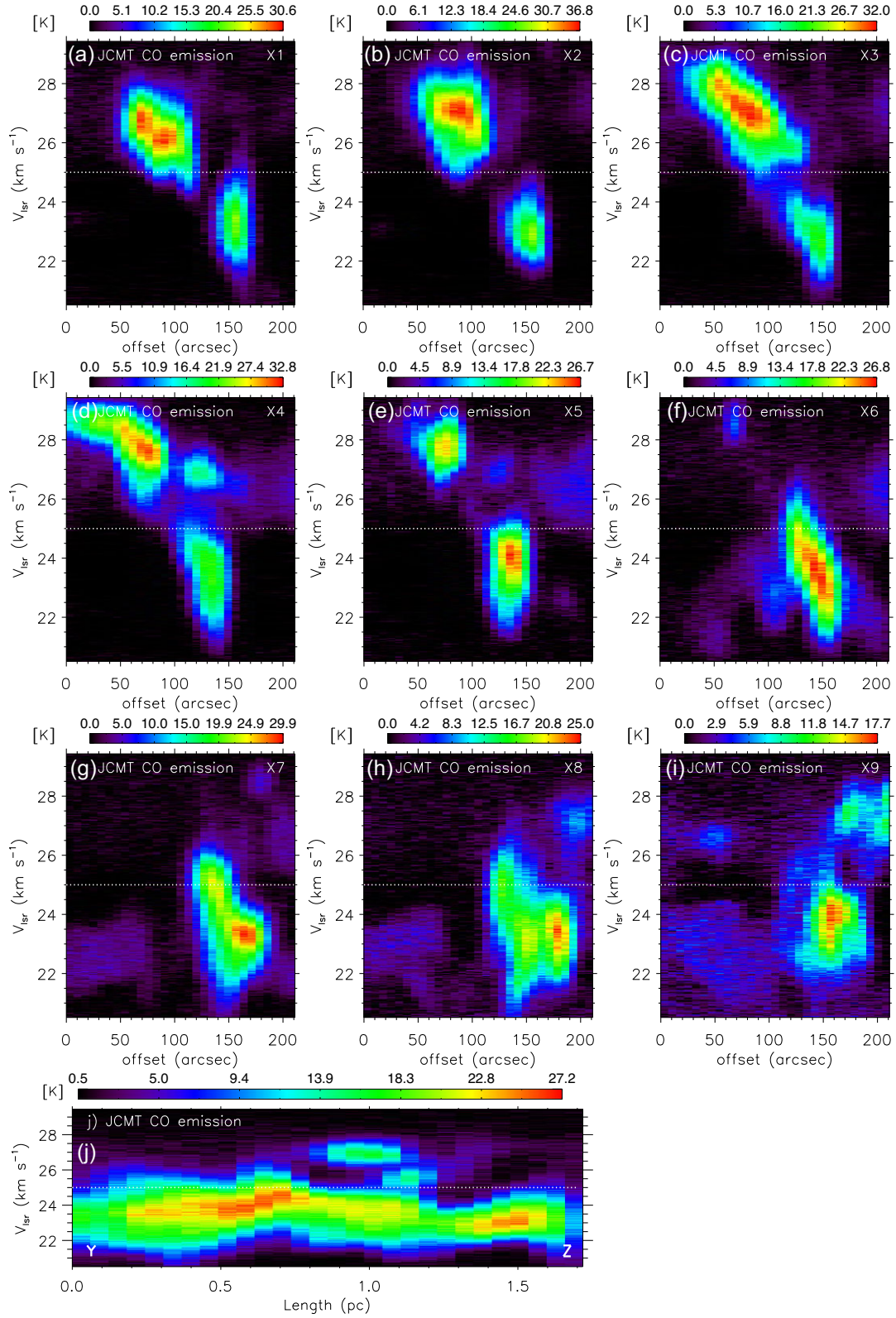
Figure 12. Position-velocity diagrams of the JCMT CO($J = 3–2$) emission along arrows (a) 'X1'; (b) 'X2'; (c) 'X3'; (d) 'X4'; (e) 'X5'; (f) 'X6'; (g) 'X7'; (h) 'X8'; (i) 'X9'; and j) the curve 'YZ' (see Fig. 9b). In each panel, the dotted line at V$_{lsr}$ = 25 km s^{-1} is shown.
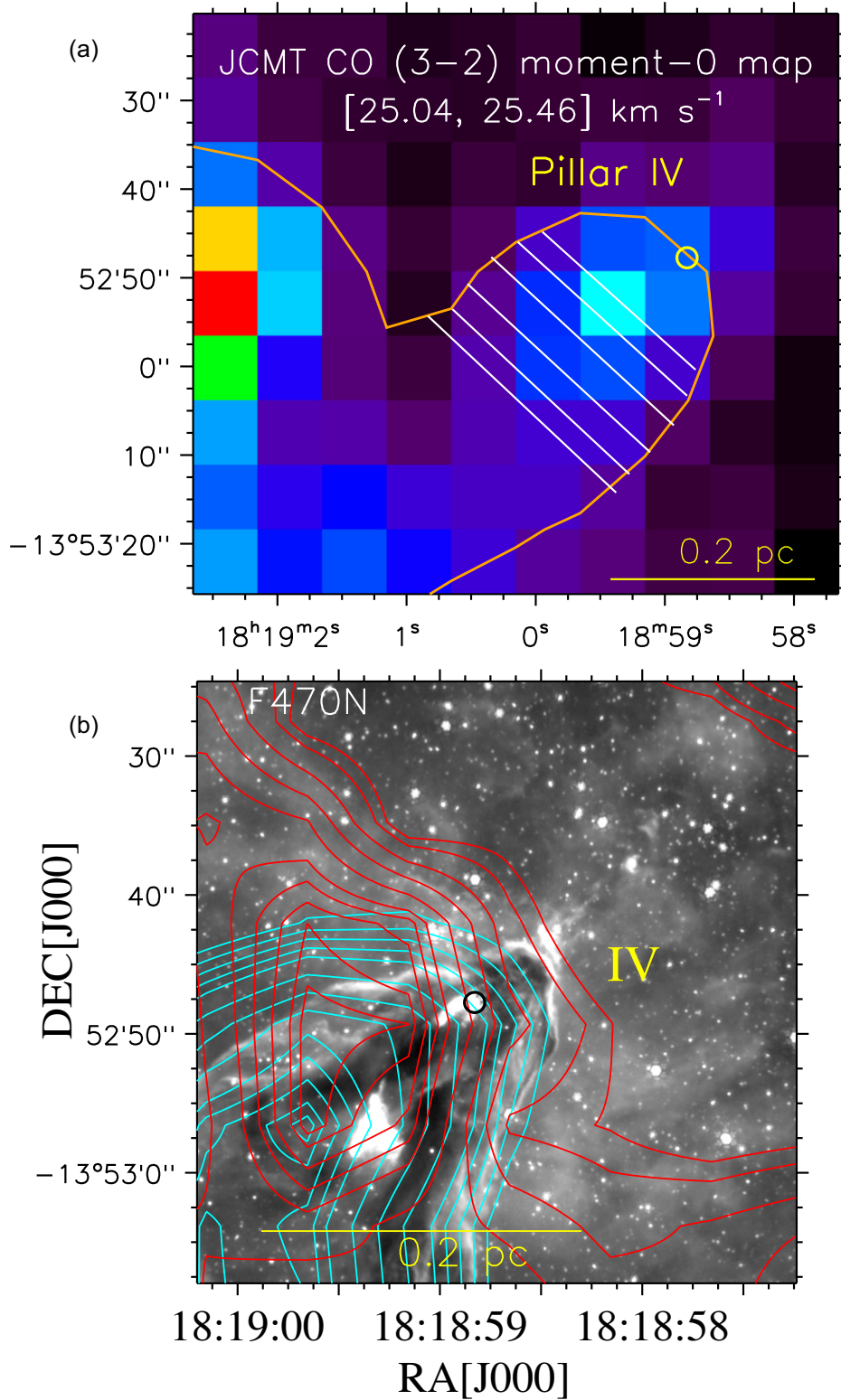
Figure 13. (a) JCMT CO(J = 3–2) integrated intensity map for the intermediate velocity range (i.e. [25.04, 25.46] km s^{-1}) towards Pillar IV for an area highlighted by the dot–dashed box in Fig. 9(d). The orange contour is at 6σ level, where, 1σ ~0.1 K km s^{-1}. Six lines (in white) used to determine the half-width/radius of the shock compressed layer are marked towards Pillar IV. (b) Distribution of the JCMT CO(J = 3–2) emission at [25.49, 29.40] and [20.51, 25.01] km s^{-1} towards Pillar IV (see the solid box in Fig. 9d). The cyan contours at [20.51, 25.01] km s^{-1} are 56.14 × (0.2, 0.25, 0.3, 0.35, 0.4, 0.5, 0.6, 0.7, 0.8, 0.85, 0.9, 0.95, and 0.98) K km s^{-1}.The red contours at [25.49, 29.40] km s^{-1} are 5.59 × (0.35, 0.4, 0.5, 0.6, 0.7, 0.8, 0.85, 0.9, 0.95, and 0.98) K km s^{-1}. The circle represents the location of the driving source of the previously reported outflow and a scale bar corresponding to 0.2 kpc at a distance of 1.74 kpc is drawn in each panel.

and the shocked interface layer (Haworth et al. 2015a, b; Torii et al. 2017). Moreover, we expect a complementary distribution in the CCC event, aligning with the spatial correlation of 'key/intensity-enhancement' and 'cavity/keyhole/intensity-depression' characteristics (e.g. Fukui et al. 2018; Dewangan et al. 2018b; Enokiya, Torii & Fukui 2021).

In Section 3.2, the analysis of the FUGIN and JCMT molecular line data has revealed similar observational signposts as expected in the collision of molecular clouds. In the direction of Pillar IV, two cloud components around 23 and 26 km $^{-1}$ and the complementary distribution of these components are investigated without any spatial displacement. A spatial match of the component around 23 km $^{-1}$ (i.e. 'key/intensity-enhancement') and the component around 26 km s^{-1} (i.e. 'cavity/keyhole/intensity-depression') is investigated (see Section 3.2 for more details). Additionally, we also find almost a V-like velocity structure and a possible bridge-like feature in the position-velocity diagrams of the JCMT CO($J = 3$–2) emission (see also Maity et al. 2022). All these observational features favour that the gas at different velocities might have collided and does not appear to be simply superposed along the line of sight.

4.2.1 Estimation of collision time-scale

For a collisional velocity of v_{col} between molecular clouds with an initial density n_1 and the magnetic field component perpendicular to the axis of collision B_1, the shock compression ratio is given by Fukui et al. (2021) as follows,

$$\frac{n_2}{n_1} = \frac{B_2}{B_1} \simeq 17 \left(\frac{v_{col}}{10 \text{ km s}^{-1}} \right) \left(\frac{B_1}{10 \, \mu G} \right)^{-1} \left(\frac{n_1}{300 \text{ cm}^{-3}} \right)^{1/2} \quad (1)$$

Here, n_2 and B_2 correspond to the final density and magnetic field component perpendicular to the axis of collision, respectively. As discussed in Maity et al. (2023), the requirement of zero spatial shift for the complementary distribution hints that the angle between the line of observation and axis of collision $\sim$0 degree (see also Fukui et al. 2018, 2021). Therefore, in our current study, the value of v_{col} is $\sim \frac{3.0}{\cos 0^\circ}$ km s^{-1} $= 3$ km s^{-1}. By employing the Chandrasekhar-Fermi methodology (Chandrasekhar & Fermi 1953), Pattle et al. (2018) estimated the plane of sky magnetic field strength for the 'Pillars of Creation', which ranges from 170 to 320 μG. Hence, it is safe to choose $B_2 = 200$–300 μG (after collision) and $B_1 = 10$ μG (before collision; Crutcher 2012). Now, following equation (1) we find $\frac{n_2}{n_1} = 20$–30, and $n_1 \sim 4.6$–10×10^3 cm^{-3}. After the initial collision between two clouds, the onset of gravitational instability can be estimated using the following equation (e.g. Whitworth et al. 1994; Fukui et al. 2021):

$$t_{start} \sim 0.5 \frac{\left(\frac{c_s}{0.2 \text{ km s}^{-1}} \right)^{1/2}}{\left(\frac{n_1}{300 \text{ cm}^{-3}} \right)^{1/2} \left(\frac{v_{col}}{10 \text{ km s}^{-1}} \right)^{1/2}} \text{ Myr.} \quad (2)$$

In this equation, c_s represents the sound speed in the molecular cloud before the collision. Using $c_s = 0.2$ km s^{-1}, $v_{col} = 3$ km s^{-1}, and $n_1 \sim 4.6$–10×10^3 cm^{-3} in equation (2), we find that t_{start} falls within the range of 0.15–0.23 Myr. Drawing from the approach introduced by Henshaw et al. (2013), the collision time-scale (t_{col}) can be determined using the following equation:

$$t_{col} \sim 2.0 \left(\frac{R_f}{0.5 \text{ pc}} \right) \left(\frac{v_{col}}{5 \text{ km s}^{-1}} \right)^{-1} \left(\frac{n_2/n_1}{10} \right) \text{ Myr,} \quad (3)$$

where R_f is the radius or half-width of the higher density region created through the collision event. In the direction of Pillar IV,

we determined the value of R_f using the JCMT CO($J = 3$–2) integrated intensity map for the intermediate velocity range [i.e. (25.04, 25.46) km s^{-1}], which corresponds to the bridge feature. The value of R_f is determined to be $\sim$0.113 pc, which is calculated as half of the average length of the lines marked on Pillar IV (see Fig. 13a). With our estimated values for $\frac{n_2}{n_1}$, v_{col}, and R_f, the resulting collision time-scale, t_{col}, is computed in a range of [1.5, 2.3] Myr. Notably, this time-scale roughly equals or exceeds the combined values of the previously reported age of M16 and the time-scale for the onset of gravitational instability following the collision event.

The *JWST* images show the presence of an isolated Class I protostar in the Pillar IV, and the mean age of a Class I protostar has been reported to be $\sim$0.44 Myr (Evans Neal J. et al. 2009). As highlighted earlier, we cannot ignore the formation of the Pillar IV by radiative compression/ablation similar to Pillars I, II, and III (e.g. Karim et al. 2023). In this context, the embedded YSO driving HH 216 may be formed by radiative implosion or the feedback of massive stars (see Karim et al. 2023, for more details). However, our results also suggest that the interaction of molecular cloud components might have influenced star formation activity in Pillar IV.

5 SUMMARY AND CONCLUSIONS

The present work uses multiscale and multiwavelength data sets to probe ongoing physical processes towards the Pillar IV and the ionized knot HH 216 in Eagle nebula (M16; d $\sim$1.74 kpc). A bipolar outflow (extent $\sim$1.6 pc at a distance of 1.74 kpc) has been reported, and the outflow-driving source is identified as a Class I protostar embedded in Pillar IV. HH 216 has been recognized as the bow shock of the red-shifted outflow lobe and is associated with the radio continuum emission. This protostar is observed as a single, isolated object (below 1000 au) in the *JWST* NIR and MIR images (resolution $\sim$0$''$.07–0$''$.7). Using the *JWST* F444W/F335M image, the outer boundary of Pillar IV is depicted with the 3.3 μm PAH emission. HH 216 is found to be associated with the 4.05 μm Brα emission in the *JWST* F444W/F335M image and the radio 4.89 and 8.71 GHz continuum emission. However, it is not detected with the 4.693 μm H$_2$ emission in the *JWST* F470N$-$F444W image. Using the NVAS radio 4.89 and 8.71 GHz continuum maps, we have produced the radio spectral index, indicating that HH 216 appears to be associated with both thermal and non-thermal radio emission. High-resolution *JWST* and HST images uncover entangled ionized structures (below 3000 au) towards HH 216, which seem to be positioned near termination shocks. The *JWST* F470N$-$F444W image has allowed us to identify new knots associated with the 4.693 μm H$_2$ emission, which are distributed towards the northern side of Pillar IV. This particular finding favours the previously proposed hypothesis of episodic accretion in the powering source of HH 216. On the southern side of the driving source, an ionized feature (extent $\sim$0.16 pc) or one of the parts of the jet is investigated. The ionized emission can be an outcome of the interplay between the shocks in the jet with its surroundings.

Using the JCMT CO($J = 3$–2), FUGIN ^{12}CO($J = 1$–0), and FUGIN ^{13}CO($J = 1$–0) emission, observational signposts of CCC towards the Pillar IV are probed, which are the connection of two cloud components (around 23 and 26 km $^{-1}$) in both physical and velocity space, a bridge-like feature, a complementary distribution of cloud components, and a possible V-like velocity structure. Overall, our findings imply that star formation activity in Pillar IV may have been impacted by the interaction of molecular cloud components between 23 and 26 km s^{-1}, which may have happened $\sim$1.5–2.3 Myr ago.

DATA AVAILABILITY

The NVAS radio continuum data underlying this article are available from the publicly accessible server.[1] The FUGIN molecular line data underlying this article is available from the website of the VizieR Service.[2] The SCUBA-2 850 µm map and HARP CO line data underlying this article are available from the publicly accessible JCMT science archive.[3] The *Herschel* column density and temperature maps underlying this article are available from the publicly accessible website.[4] The *Spitzer* images underlying this article are available from the publicly accessible NASA/IPAC infrared science archive.[5] The *JWST* images underlying this article are available from the publicly accessible MAST archive.[6] The HST F657N image underlying this article is available from the publicly accessible JCMT science archive.[7]

REFERENCES

Anathpindika S. V., 2010, MNRAS, 405, 1431
Andersen M., Knude J., Reipurth B., Castets A., Nyman L. Å., McCaughrean M. J., Heathcote S., 2004, A&A, 414, 969
Anglada G., Rodríguez L. F., Carrasco-González C., 2018, A&A Rev., 26, 3
Astropy Collaboration, 2013, A&A, 558, A33
Astropy Collaboration, 2018, AJ, 156, 123
Balfour S. K., Whitworth A. P., Hubber D. A., 2017, MNRAS, 465, 3483
Beichman C. A., Rieke M., Eisenstein D., Greene T. P., Krist J., McCarthy D., Meyer M., Stansberry J., 2012, in Clampin M. C., Fazio G. G., MacEwen H. A., Oschmann Jacobus M. J., eds, Proc. SPIE Conf. Ser. Vol. 8442, Space Telescopes and Instrumentation 2012: Optical, Infrared, and Millimeter Wave. SPIE, Bellingham, p. 84422N
Benjamin R. A. et al., 2003, PASP, 115, 953
Bisbas T. G., Tanaka K. E. I., Tan J. C., Wu B., Nakamura F., 2017, ApJ, 850, 23
Bonatto C., Santos J. F. C. J., Bica E., 2006, A&A, 445, 567
Buckle J. V. et al., 2009, MNRAS, 399, 1026
Chandrasekhar S., Fermi E., 1953, ApJ, 118, 113
Crossley J. H., Sjouwerman L. O., Fomalont E. B., Radziwill N. M., 2007, in American Astronomical Society Meeting Abstracts. p. 132.03
Crutcher R. M., 2012, ARA&A, 50, 29
Dewangan L. K., Ojha D. K., 2017, ApJ, 849, 65
Dewangan L. K., Ojha D. K., Zinchenko I., Janardhan P., Luna A., 2017, ApJ, 834, 22
Dewangan L. K., Ojha D. K., Zinchenko I., Baug T., 2018a, ApJ, 861, 19
Dewangan L. K., Dhanya J. S., Ojha D. K., Zinchenko I., 2018b, ApJ, 866, 20
Dewangan L. K., Ojha D. K., Sharma S., Palacio S. d., Bhadari N. K., Das A., 2020, ApJ, 903, 13
Dewangan L. K., Maity A. K., Mayya Y. D., Bhadari N. K., Bhattacharyya S., Sharma S., Banerjee G., 2023, preprint (arXiv:2309.13351)
Dhanya J. S., Dewangan L. K., Ojha D. K., Mandal S., 2021, PASJ, 73, S355
Enokiya R., Torii K., Fukui Y., 2021, PASJ, 73, S75
Evans Neal J. I. et al., 2009, ApJS, 181, 321
Flagey N., McLeod A. F., Aguilar L., Prunet S., 2020, A&A, 635, A111
Fukui Y. et al., 2014, ApJ, 780, 36
Fukui Y. et al., 2018, ApJ, 859, 166
Fukui Y., Habe A., Inoue T., Enokiya R., Tachihara K., 2021, PASJ, 73, S1
Getman K. V., Feigelson E. D., Garmire G., Broos P., Wang J., 2007, ApJ, 654, 316
GLIMPSE Team, 2020, GLIMPSE I Archive. available at: https://catcopy.ipac.caltech.edu/dois/doi.php?id = 10.26131/IRSA210
Habe A., Ohta K., 1992, PASJ, 44, 203
Hartmann L., Megeath S. T., Allen L., Luhman K., Calvet N., D'Alessio P., Franco-Hernandez R., Fazio G., 2005, ApJ, 629, 881
Haworth T. J. et al., 2015a, MNRAS, 450, 10
Haworth T. J., Shima K., Tasker E. J., Fukui Y., Torii K., Dale J. E., Takahira K., Habe A., 2015b, MNRAS, 454, 1634
Healy K. R., Hester J. J., Claussen M. J., 2004, ApJ, 610, 835
Henshaw J. D., Caselli P., Fontani F., Jiménez-Serra I., Tan J. C., Hernandez A. K., 2013, MNRAS, 428, 3425
Hester J. J. et al., 1996, AJ, 111, 2349
Hunter J. D., 2007, Comput. Sci. Eng., 9, 90
Indebetouw R., Robitaille T. P., Whitney B. A., Churchwell E., Babler B., Meade M., Watson C., Wolfire M., 2007, ApJ, 666, 321
Inoue T., Fukui Y., 2013, ApJ, 774, L31

---

[8]https://archive.stsci.edu/doi/resolve/resolve.html?doi = 10.17909/r4d5-d269
[9]http://www.astropy.org
[1]http://www.vla.nrao.edu/astro/nvas/
[2]https://nro-fugin.github.io/release/
[3]https://www.cadc-ccda.hia-iha.nrc-cnrc.gc.ca/en/jcmt/
[4]http://www.astro.cardiff.ac.uk/research/ViaLactea/
[5]https://irsa.ipac.caltech.edu/frontpage/

[6]https://archive.stsci.edu/missions-and-data/jwst
[7]https://archive.stsci.edu/missions-and-data/hst/

Karim R. L. et al., 2023, SOFIA FEEDBACK Survey: The Pillars of Creation in [C II] and Molecular Lines. preprint (arXiv:2309.14637)

Kohno M. et al., 2018, PASJ, 70, S50

Kuhn M. A., Hillenbrand L. A., Sills A., Feigelson E. D., Getman K. V., 2019, ApJ, 870, 32

Lei Z. et al., 2023, ApJ, 954, 130

Linsky J. L., Gagné M., Mytyk A., McCaughrean M., Andersen M., 2007, ApJ, 654, 347

Longair M. S., 1992, High energy astrophysics. Vol.1: Particles, photons and their detection.

Maity A. K., Dewangan L. K., Sano H., Tachihara K., Fukui Y., Bhadari N. K., 2022, ApJ, 934, 2

Maity A. K., Dewangan L. K., Bhadari N. K., Ojha D. K., Chen Z., Pandey R., 2023, MNRAS, 523, 5388

Marsh K. A., Whitworth A. P., Lomax O., 2015, MNRAS, 454, 4282

Marsh K. A. et al., 2017, MNRAS, 471, 2730

Meaburn J., White N. J., 1982, MNRAS, 199, 121

Meaburn J., Whitehead M. J., 1990, A&A, 235, 395

Molinari S. et al., 2010a, PASP, 122, 314

Molinari S. et al., 2010b, A&A, 518, L100

Nishimura A. et al., 2021, PASJ, 73, S285

Oliveira J. M., 2008, in Reipurth B., ed., Handbook of Star Forming Regions, Vol. 5, Volume II. p. 599

Padovani M., Hennebelle P., Marcowith A., Ferrière K., 2015, A&A, 582, L13

Padovani M., Marcowith A., Hennebelle P., Ferrière K., 2016, A&A, 590, A8

Pattle K. et al., 2018, ApJ, 860, L6

Pontoppidan K. M. et al., 2022, ApJ, 936, L14

Pound M. W., 1998, ApJ, 493, L113

Priestley F. D., Whitworth A. P., 2021, MNRAS, 506, 775

Reiter M., Morse J. A., Smith N., Haworth T. J., Kuhn M. A., Klaassen P. D., 2022, MNRAS, 517, 5382

Rieke M. J., Kelly D., Horner S., 2005, in Heaney J. B., Burriesci L. G., eds, Proc. SPIE Conf. Ser. Vol. 5904, Cryogenic Optical Systems and Instruments XI. SPIE, Bellingham, p. 1

Rieke G. H. et al., 2015, PASP, 127, 584

Rigby J. et al., 2023, PASP, 135, 048001

Rybicki G. B., Lightman A. P., 1979, Radiative processes in astrophysics, A Wiley-Interscience Publication, New York

Sofue Y., 2020, MNRAS, 492, 5966

Spitzer Science C., 2009, VizieR Online Data Catalog. p. II/293

Torii K. et al., 2011, ApJ, 738, 46

Torii K. et al., 2015, ApJ, 806, 7

Torii K. et al., 2017, ApJ, 835, 142

Tremblin P. et al., 2013, A&A, 560, A19

Umemoto T. et al., 2017, PASJ, 69, 78

White G. J. et al., 1999, A&A, 342, 233

Whitworth A. P., Bhattal A. S., Chapman S. J., Disney M. J., Turner J. A., 1994, MNRAS, 268, 291

Wright G. S. et al., 2015, PASP, 127, 595

This paper has been typeset from a TEX/LATEX file prepared by the author.